



**CENTRO DE INVESTIGACIONES
EN OPTICA, A.C.**

CENTRO DE INVESTIGACIONES EN ÓPTICA A.C.

UV TO RED UPCONVERSION EMISSION
FROM ERBIUM YTTERBIUM CODOPED
BARIUM ZIRCONATE

THESIS SUBMITTED IN PARTIAL FULFILLMENT OF THE
REQUIREMENTS FOR THE DEGREE OF MASTER IN SCIENCE (OPTICS)
AT CENTRO DE INVESTIGACIONES EN ÓPTICA

by

José Samuel Pérez Huerta

Advised by

L. A. Díaz-Torres

and

P. Salas Castillo

León Gto., México.

July 2007

Research Supervisor:

Dr. Luís Armando Díaz-Torres
(DEPARTMENT OF PHOTONICS, CIO)

Internal Reviewer:

Dr. Luís Manuel Arévalo Aguilar
(DEPARTMENT OF PHOTONICS, CIO)

External Reviewer:

Dr. Pedro Salas Castillo
(INSTITUTO MEXICANO DEL PETRÓLEO)

Acknowledges

Special acknowledges to:

My advisor Dr. Luís Armando Díaz-Torres for the supervising and guiding.
My coadvisor Dr. Pedro Salas Castillo, Dr. Carlos Angeles Chávez , at I.M.P., for
their support with the synthesis and XRD, TEM, and HRTEM characterization.
MI. Ruth Ivonne Mata Chavéz for her invaluable help in the English redaction of
this manuscript.
CONACyT as this work is supported by its scholarship.
The Nanoscience CIO group.
Authorities and Teachers of CIO.
My classmates.

Abstract

Visible upconversion emission of Er^{3+} in nanocrystalline BaZrO_3 (BZO) powder is obtained under IR excitation in the range between 900 to 1050 nm. In single Er^{3+} doped BaZrO_3 the blue emission was neglected and when Yb^{3+} is added then it acts as a sensitizer. The BZO was prepared by a hydrothermal process at low temperature (100°C). The synthesized nanocrystalline cubic perovskite phase remains stable under subsequent annealing treatment up to 1000°C . Additional or different crystalline phases or segregation were not detected. Green and red emissions of Er^{3+} are enhanced in the codoped samples of $\text{Yb}^{3+} - \text{Er}^{3+}$ by three orders of magnitude. The blue emission depends on both excitation power and pump wavelength. It is the first time that upconversion emission is observed in a BaZrO_3 matrix. A possible mechanism for the UV to red emission under NIR excitation is discussed based on experimental results.

Contents

1	Antecedents	1
1.1	Introduction	1
1.2	Barium Zirconate	4
1.3	Rare Earths Generalities	5
1.3.1	Symmetry considerations	7
1.3.2	Terms Symbol	7
1.3.3	Judd-Ofeldt theory	7
1.3.4	Phonon interaction	8
1.3.5	Ion-Ion Interaction	9
1.3.6	Cooperative luminescence	9
1.3.7	Cooperative upconversion	10
1.3.8	Energy migration	11
1.3.9	Cross relaxation	11
1.3.10	Excited state absorption	11
1.3.11	Electronic configuration of Rare Earths	12
2	Synthesis, Structure and Morphology of BZO	18
2.1	BaZrO ₃ Nanocrystallites Synthesis	18
2.1.1	Hydrothermal Process	19
2.2	Structure and Morphology	19
2.2.1	X-Ray Diffraction	19
2.2.2	SEM, TEM and HRTEM	24
2.3	Infra-Red Fourier Spectroscopy	30
3	Optical Spectroscopy	32
3.1	Absorption Spectroscopy	32
3.1.1	Absorption Spectroscopy Procedure	33
3.1.2	Absorption Spectroscopy Results	33
3.2	Emission Spectroscopy	36
3.2.1	Emission Spectroscopy Procedure	37
3.2.2	Emission Spectroscopy Results and Discussions	38

4	Conclusions	47
A	Barium Zirconate Face Ending	49
B	Additional XRD Results and Discussion	52
C	Energy Dispersive X-ray Spectroscopy (EDXS)	54

Chapter 1

Antecedents

1.1 Introduction

Nanometric phosphors doped with Rare-Earths (RE) has been carefully studied as the reduction of the particle size of crystalline systems could modify significantly some of their bulk properties, such as higher luminescent efficiency and better resolution in lighting and display applications [1, 2, 3, 4].

Up to now, many RE-doped nanocrystalline systems have been obtained by means of diverse synthesis methods and their corresponding luminescent properties have been studied. Using the available near-infrared (NIR) pump sources, such as solid-state lasers and semiconductor laser diodes, many of NIR to visible upconversion emission processes and various energy transfer processes have been reported.

Trivalent Erbium (Er^{3+}) has excellent up-conversion properties. Besides, the addition of Yb^{3+} as a sensitized mechanism, has made possible to greatly increase the up conversion efficiency of $\text{Yb}^{3+} - \text{Er}^{3+}$ codoped systems. A better performance of Er^{3+} in nanosized environments is an active research area and, in particular, the search of new host materials with small multiphonon decay rates and structural and chemical stability under corrosive environments and wide range of temperatures.

Trivalent Ytterbium (Yb^{3+}) ion has been used ideally for diode pumping since it has the simplest energy level scheme, between R.E. active ions, consisting in only two levels: the $^2\text{F}_{5/2}$ excited state and the $^2\text{F}_{7/2}$ ground state. This simple energy scheme results in several advantages (for laser applications) as compared with the one of Nd^{3+} ion. These are a no excited state of absorption, no absorption in the visible range (i.e. transparent), no cross relaxation process and no up-conversion or any internal mechanism that reduces the effectiveness of the laser performance. However, Yb^{3+} is the less shielded RE because of its almost filled $4f$ shell and thus Ytterbium can interact with the crystal field in a significative way.

The rare earth ion that has practical interest is the trivalent Er^{3+} ion because its $4f - 4f$ transition in the $1.53 \mu\text{m}$ emission peak, ($^4\text{I}_{13/2} \rightarrow ^4\text{I}_{15/2}$), has a fortunate

CHAPTER 1. ANTECEDENTS

1.1. INTRODUCTION

coincidence with the minimal loss window of silica fibre for optical telecommunications. This “ultra low loss window” is in the range of 1450-1600 nm. This has lead to use Er doped material as gain elements and sources in communications systems. For instance, nowadays Erbium doped fibre amplification is being developed as larger bandwidths are demanded [5, 6]. Also, the $4f^{n-1} \rightarrow 5d^1$ transitions are being usual in x-ray detection [7, 8], but the high energy involved is beyond the interest in this work.

The main interest in RE doped nanostructured materials is in photonic applications such as up-conversion lasing, optoelectronic displays and two photon imaging in con-focal microscopy. It is observed that all of them involve IR to visible up conversion.

Practical phosphors from ultraviolet to green emission spectral range have a wide range of applications such as: high-density optical storage, color displays, optical fiber communications, biomedicine (biological labeling) and infrared sensor [9].

Nevertheless, if a short-wavelength emission is required in a phosphor matrix, the host material could be a considerable problem itself. So, special attention should be paid in the election of the crystalline environment.

The host must be selected based on the fluorescence performance of active ions. A low lattice phonon reduces the nonradiative decay multiphonon relaxations and thus improves the up conversion emission.*

In particular, referred to biological labeling, these are applied as single virus tracing, ion channel detection, gene delivery, DNA sequence and frequency resonance energy transfer, etc. The general request for these labels are water solubility (characteristic given by the host), biocompatibility (nontoxic, penetrating cells and organelle), monodispersive size distribution and nanometric size. As an example, organic dyes and fluorescent proteins have been used as traditional labels but they have a practical problem of photobleaching due to a photochemical reaction [10].

In the same way, inorganic quantum dots suffer from high autofluorescence and scattering of excitation light in the ultraviolet (UV) range. On the other hand, RE up-conversion fluorescent labels do not have those limitations since they have stable fluorescence in the visible range and the excitation can be done by low cost continuous wave near infrared commercial diode lasers. In usual multiphoton imaging process (i.e. two photon confocal imaging) an expensive mode locked near the infrared has to be used.

Multicolor labels are used to identify different cells or molecules, narrow emission is request, but in general RE ions emit several emission lines at the same time. Wavelength tunability has been achieved by different procedures. One of the most practical is the saturation and quenching of certain RE ions levels when the dopant concentration is changed. For example, red or green emission is obtained when the

*For instance, for ZrO_2 the phonon energy is about 470 cm^{-1} and for the fluoride is 400 cm^{-1}

CHAPTER 1. ANTECEDENTS

1.1. INTRODUCTION

Er – Yb concentration is varied. In [10], the concentration of Er(1 mol %) and Yb(0.5 mol %) gives essentially green luminescence whereas the concentration of Er(1 mol %) and Yb(2 mol %) gives mainly red luminescence. Briefly, the up conversion dynamics can be manipulated in order to get the wanted emission [11, 12].

Frequency up-conversion is the third nonlinear optical process most widely investigated, after second harmonic generation (SHG) and two photon absorption, in the two last decades. Upconversion (UC) has the advantage to be a very efficient process that converts long-wavelength excitation radiation into short wavelength output radiation [13].

While UC needs the existence of at least two real metastable emitting states, SHG and two-photon absorption do not, such processes are explained using virtual levels. See Fig.1.1. Thus, UC process has the highest relative efficiency. This fact is due to the resonances involved for in- and outgoing photons. In order to achieve highest efficiency, the photons have to interact with the ions a longer time. This is accomplished by the existence of resonances. So, UC is the most efficient because it is closer to the full resonance case [14].

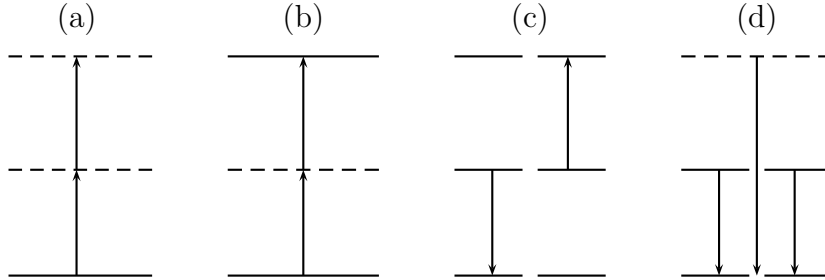


Figure 1.1: Important nonlinear optical processes: (a) Second harmonic generation; (b) Two photon absorption; (c) Up conversion; (d) Cooperative emission. In all cases, incident photons are of ω frequency and output photons are of 2ω .

The up conversion process is possible by two mechanisms: Excited state absorption (ESA) and energy transfer (i.e. as up conversion and cross relaxation) mechanisms. The first process increases as both the irradiating density excitation and the lifetime of the excited state is increased. Whereas the energy transfer processes become important as the dopant concentration is enhanced.

The overall performance of any RE-doped nanocrystal depends on the dynamics of the active ions and their interactions with the host material. The interaction can be a function of the host phase, the dopant concentration, energy migration, the statical distribution of the active ions and the symmetry in the host.

Quantum confinement due to the host particle size does not occur in RE doped

CHAPTER 1. ANTECEDENTS

1.2. BARIUM ZIRCONATE

oxide nanocrystallites because the $4f - 4f$ visible transitions involve electrons in the atomic orbitals of the active ions. Therefore, the electrons are well localized and their quantum behavior is only dependent on the condition of the atomic ion configuration and weakly on the crystalline host environment.

Therefore, intrinsic luminescence lifetime can be modified as:

$$\tau = \frac{1}{W_{RAD} + W_{NT} + W_{ET}}, \quad (1.1)$$

where W_{RAD} is the radiative photon emission rate, W_{NT} is the nonradiative (multi-phonon) emission rate and W_{ET} is the energy transfer between neighboring RE ions. In the dipole-dipole interaction, the last term depends on the inverse of the sixth power of the interatomic distance between donor and acceptor. It increases as the concentration raises [3, 13]. The radiative emission rate is governed by the lattice morphology and the site symmetry whereas the nonradiative rate is function of the host phonon spectrum that can be modified by phase and the size of the particle (significantly in the nanometric scale host).

1.2 Barium Zirconate

Perovskite materials offer excellent optical, electrical, chemical and structural properties and they are capable of hosting ions of various sizes. Oxides (such as YAlO_3 , BaTiO_3 , LiNbO_3) and fluorides (such as KMgF_3 and NaYF_4) have been used in important applications as visible emitting phosphors.

A common problem with fluorides -even when they have the lowest phonon energies (for instance, NaYF_4), and in consequence the best up-conversion efficiencies- is the lack of chemical stability. Besides, in many cases they are hygroscopic, which is problematic when it's used in biological applications or systems subject to wet environments. On the other hand, oxides are quite resistant to corrosive environments and have good optical properties. However, most of the perovskites have temperature phase transformations that surface the refraction index anisotropies and therefore, non linear optical phenomena such as second harmonic generation [15]. In high energy applications, such change could be detrimental since the generated heat can lead to induced anisotropies and thus limit the range of pump power [16]. The competition between SHG and cooperative emission is due to maximized anisotropies by one particular phase. The cooperative process is reduced by the sites occupied by Yb ions. But the inverse situation is originated when the crystalline phase shifts and thus anisotropies fade out. Then Yb ions occupy other lattice sites that improve the cooperative interaction between RE ions.

Barium zirconate (BaZrO_3 , BZO) is a promising refractory ceramic structural material with a very high melting point (2600 °C) and a low chemical reactivity

towards corrosive compounds. It belongs to perovskite family of the type $A^{2+} B^{4+} C^{6-}$. BZO is a cubic oxide perovskite that does not follow phase transitions within the range between 4K and 1600K [17]. Because of this, BZO has been used in high temperature superconductor applications. Electroceramic applications have been done with BZO.

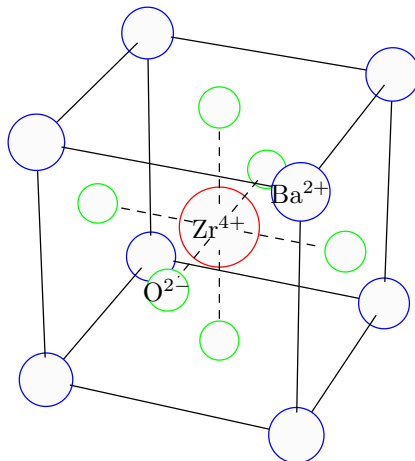


Figure 1.2: A cubic perovskite $BaZrO_3$ unit cell.

The crystalline space group of BZO perovskite is $Pm\bar{3}m$ and the ideal unit cell is shown in Fig. 1.2. In addition, BZO has attracted attention as a promising candidate for protonic electrolytes in fuel cell applications [18]. In this work it is presented a relative easy hydrothermal method for the synthesis of regular and homogeneous $BaZrO_3$ nanocrystallites. Blue, green and red visible emission is explored from Yb – Er codoped BZO under NIR excitation. The photoluminescence results suggest that $Er^{3+} - Yb^{3+}$ codoped nanocrystalline $BaZrO_3$ is a good candidate for blue light generation via up-conversion processes and therefore it is a good candidate for biological labeling under NIR excitation, as well as for white lighting applications via up-conversion processes.

1.3 Rare Earths Generalities

Rare earths, also referred as lanthanides, are in the sixth row of the periodic table. They go from Lanthanum to Ytterbium (see Table 1.1). The main electronic characteristic of rare earths are their partially filled $4f$ shell that is shielded by the external cores of $5s^2$ and $5p^2$ electrons. Thus, the energy levels of RE are extremely insensitive to the external environment (crystalline field) in which they are placed.

CHAPTER 1. ANTECEDENTS

1.3. RARE EARTHS GENERALITIES

Z	Element	Configuration
57	La	$[\text{Xe}]6s^24f^1$
58	Ce	$[\text{Xe}]6s^24f^2$
59	Pr	$[\text{Xe}]6s^24f^3$
60	Nd	$[\text{Xe}]6s^24f^4$
61	Pm	$[\text{Xe}]6s^24f^5$
62	Sm	$[\text{Xe}]6s^24f^6$
63	Eu	$[\text{Xe}]6s^24f^7$
64	Gd	$[\text{Xe}]6s^24f^8$
65	Tb	$[\text{Xe}]6s^24f^9$
66	Dy	$[\text{Xe}]6s^24f^{10}$
67	Ho	$[\text{Xe}]6s^24f^{11}$
68	Er	$[\text{Xe}]6s^24f^{12}$
69	Tm	$[\text{Xe}]6s^24f^{13}$
70	Yb	$[\text{Xe}]6s^24f^{14}$

Table 1.1: Electronic configuration of rare earths (ground state), where Xenon configuration is: $[\text{Xe}] = 1s^22s^22p^63s^23p^64s^23d^{10}4p^65s^24d^{10}5p^6$

This also explains the remarkable similarity of their chemical properties and the reason why they are located in a single column (III B) in the periodic table [19, 20].

When RE are incorporated in crystalline or amorphous hosts, they exist as trivalent ion ($3+$) or sometimes as divalent ions ($2+$)[†]. Trivalent RE ions emit almost as free ions, that is, they exhibit intense narrow-band intra $-4f$ luminescence in a large variety of hosts (i.e. oxides, fluorides, semiconductors, organic, etc.). The narrow behavior of RE radiative transitions in solid hosts can be explained as a consequence of the shielding provided by the $5s^2$ and $5p^2$ electrons. So, small deviations from crystalline field can be dealt with the well-known perturbation theory.

As a consequence of the shielding of the $4f$ electrons, the configuration of electronic levels are influenced much more by spin-orbit coupling interaction than by the crystalline field [22]. The intra- $4f$ transitions are partially forbidden and are made partially allowed by the crystal interaction that mixes opposite parity wavefunctions. Therefore, luminescence lifetimes are usually long (e.g. millisecond range). This feature can lead to applications of RE ions into phosphors.

In a general sense, there are two ways to excite RE ions in order to get luminescence [5]:

[†]Divalent species like Samarium and Europium (Sm, Eu) exhibit notable luminescence, but trivalent ions are of most general interest [5, 21].

Direct By means of resonant optical excitation via the interaction of photons of the adequate energy with specific RE $4f$ absorption bands, cathodoluminescence and electroluminescence, and

Indirect Carrier-mediated excitation transfer given in a semiconductor host (applied in optoelectronic devices) and dipole-dipole Förster-Dexter coupling (in insulators).

1.3.1 Symmetry considerations

Performance of RE ions in solid hosts are directly related with the specific site occupied by the ion within the lattice. This identification, except for few cases, is rather complex. This is carried out with luminescence studies combined with electron spin resonance (ESR), Zeeman and point charged calculation techniques.

1.3.2 Terms Symbol

Energy levels in RE are labeled just as their angular momentum and spin quantum numbers, using the so-called **term symbol**. It is specified by $^{2S+1}L_J$, where L refers to the total orbital angular momentum of the ion. It is obtained by combining the orbital angular momentum of the individual $4f$ electrons in the ion according to the Clebsch-Gordan series. $2S + 1$ is the number of possible orientations of the total spin of the whole ion (also referred as multiplicity of the spin) and S is the total spin of the ion. J is referred as de total momentum and is determined using the Russell-Saunders coupling scheme (see Fig.1.3).

1.3.3 Judd-Ofeldt theory

Transition probabilities or oscillator strengths between energy levels in RE ions are extremely difficult to measure experimentally, and they are frequently calculated using the Judd-Ofeldt theory. This theory states that the oscillator strength for the transition between two states $^{2S+1}L_J$ (given by the wavefunction Ψ_i) and $^{2S'+1}L'_J$ (specified by Ψ_f) is given by

$$S = \frac{1}{e^2} |\langle \Psi_f | H | \Psi_i \rangle|^2 = \sum_{k=2,4,6} \Omega_k |\langle f^N \gamma S' L' J' | U^{(k)} | f^N \gamma S L J \rangle|^2, \quad (1.2)$$

where H is the electric dipole Hamiltonian (in tensorial form $U^{(k)}$) Ω_k represents the so-called Judd-Ofeldt parameters. Here, the f^N configuration leads to values of S, L, J and the factor γ is used to distinguish electronic states that share the same values of S and L . Those coefficients describe the influence of the external crystal field on the radiative transition probabilities on the intra $4f - 4f$ transitions.

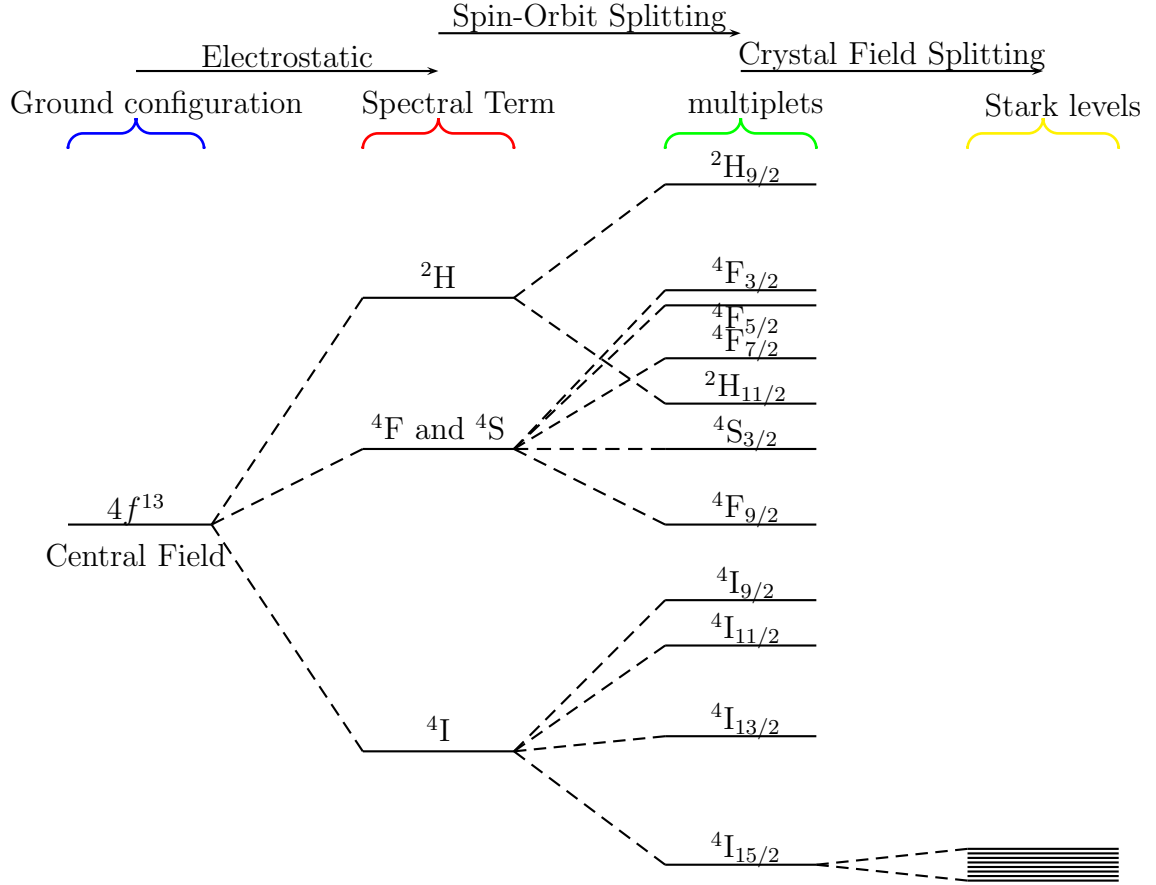


Figure 1.3: Schematic representation of Er energy diagram. There is not vertical scale but the energy increases in the upward direction. The ground state configuration of the single Er ion is divided to Stark levels owed to crystal field interactions. Here, only the splitting of the lower level is schematized for clarity.

1.3.4 Phonon interaction

Multiphonon relaxation can quickly depopulate one excited state and could lead to quench luminescence. That process is significant when a small number of phonons are required to bridge the energy gap between the upper and lower electronic states of the RE ions. As a general rule, if the band gap is so small as four times the phonon cut-off energy ($E_{phonon} > \frac{1}{4}E_{gap}$), the luminescence will be completely quenched (i.e. four or lees phonons are bridging the gap). For phonon cut-off energies between 10% and 25% of band gap, quenching will lead to temperature dependent luminescence lifetime (4 to 8 phonons are involved). Whilst for phonon cut-off energy smaller than

these (e.g. more than ten phonons), the contribution of multiphonon relaxation will be negligible (the phonon bridge is practically impossible). Then, the multiphonon process depends strongly on both the host material (the phonon spectrum) and the electronic structure of the RE (band gap). If a lower phonon host is selected (such a fluoride or tellurite glasses), the multiphonon relaxation will be reduced and this allows radiative transitions that will not be quenched[‡]

1.3.5 Ion-Ion Interaction

One remarkable characteristic of RE ions is their tendency to interact between them. These interactions can be either between ions of the same type or on different ones (i.e. as in the sensitization of RE ions by means of another different one). The former case increases non-radiative decay channels (loss mechanism) or luminescence from unwanted transitions. The latter could be employed in a novel pumping method, the excitation is provided to one kind of ion and is transferred to another. Thus, a wider range of pump sources become available [10].

1.3.6 Cooperative luminescence

The cooperative optical absorption was first announced by Varsanyai et al. in [23]. The observed phenomena was explained as a resonance interaction among neighboring ions pairs. Nakazawa in [24] made the first experimental observation of cooperative luminescence in YbPO₄: Yb when the level ²F_{7/2} is excited around 998 nm. Then, a cooperative green emission was obtained around 497 nm. This green photon is generated by a pair of Yb excited ions in a cooperative way. The successfulness of this process is dictated by the ion concentration. As concentration increases, the closer the ions are, and it is more probable its tendency to interact owed to the overlap of their electronic wavefunctions.

The cooperative emission is broader than the usual emission spectra. This is caused by the combination of the single-ion transitions between the Stark levels of the excited state (²F_{5/2} has 4 Stark-levels) and the ground state (²F_{7/2} has 3 Stark-levels).

One characteristic of cooperative emission is that its lifetime is given by half of metastable emission ($\tau_{coop} = \tau_{single}/2$). This is so, because it is considered that two near infrared photons are used to create one green emission [25]. Then the cooperative luminescence is given by

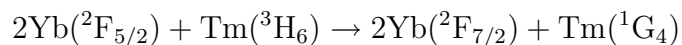
$$I_{coop} = kI_{pump}^2. \quad (1.3)$$

[‡]For instance, Erbium transitions in a glass host (but not fluorides), are non-radiative except ⁴I_{13/2} → ⁴I_{15/2}) [5].

Although within this scope, cooperative process has been related with the generation of visible emission radiation. In general this cooperative process can lead to other results. All of them have one thing in common: they all become activated under the influence of light, leading to the development of a principal phenomena whose quantum energy is greater than that of light pumping. For instance, in photographic emulsion, the photolysis reaction of silver halide needs more energy than the provided by the incident light [25]. Also in green leaves, in the photosynthesis process, chlorophyll absorbs sun light even though the reaction of detaching H from H₂O and combining it with CO₂ requires three or four times as much energy. However, when these processes have to be explained, special attention should be put in energy conservation and entropy law. Entropy of a radiation field is proportional to its frequency bandwidth and to the solid angle through which it propagates also [16].

1.3.6.1 Cooperative Sensitization of Luminescence

When ions of different species are codoped, it can happen that a pair of cooperative sensitization ions may transfer their energy simultaneously into one single acceptor ion. For instance, in the Yb – Tm codoped system, two excited Yb ions can transfer its energy into one Tm ion as it is described by transfer process [25]:



It is important to distinguish between cooperative emission and cooperative up-conversion emission. They are not the same because the former involves one virtual level and the latter entails real levels and it is a transfer process mechanism.

1.3.7 Cooperative upconversion

Ions in the metastable state, decaying to the ground state, can couple in such a way that the decay of the ion D promotes a nearby ion A into a higher level. From the upper level, ion A could decay rapidly non radiatively, radiatively, or alternatively return to a metastable level and subsequently, emits radiation. For instance, in oxide glasses the relaxation is rapidly nonradiative and hence, the result of cooperative upconversion is the loss of excitation into heat (unwanted effect).

In order to get cooperative upconversion it is necessary to have interacting ions in the metastable level. Therefore, this process becomes important at relative high dopant concentrations.

This accumulation of energy excitation process is symbolically represented as:



This process does not require a strong interaction. Because of the overlapping of the wavefunctions of the interacting ions, it can be accomplished through Coulomb multipole interaction (when $2E_{A^*} \approx E_{A^{**}}$).

1.3.8 Energy migration

An ion in the metastable state can interact with a nearby ion in its ground state raising it to an upper level. The probability of non radiative decay increases with each successive transfer (loss mechanism). Dipole-dipole Förster-Dexter interactions can be responsible for this process. Thus, energy migration is strongly related with RE ions concentration.

1.3.9 Cross relaxation

The energy transfer from one decaying ion from a higher excited state to one intermediate state can promote a neighbor ion from the ground state to a metastable level of a lower energy. Thus, the upper level is depopulated by this process and consequently, the lifetime is decreased and the emission can be quenched. Cross relaxation occurs more often at higher concentrations and the energy exchange must be quite similar.

1.3.10 Excited state absorption

When an upper state has sufficiently long lifetime, the interaction between incident photons and the excited ion can promote electrons in the metastable state to higher resonant levels with the incident photon energy. From the last level, the electron can return to a metastable state by multiphonon relaxation or radiative decay. However, two photons are necessary in that process and one of these photons has been lost as either heat or emission at a different wavelength. For optical amplification purposes, excited state absorption is a loss channel.

Erbium ion has a noticeable favorable spacing of levels [26]:

$${}^4I_{15/2} \rightarrow {}^4I_{13/2} \rightarrow {}^4I_{9/2} \rightarrow {}^4S_{3/2} \rightarrow {}^2H_{9/2} \quad \text{spaced} \sim 6500\text{cm}^{-1}$$

$${}^4I_{15/2} \rightarrow {}^4I_{11/2} \rightarrow {}^4F_{7/2} \quad \text{spaced} \sim 10,200\text{cm}^{-1}$$

$${}^4I_{15/2} \rightarrow {}^4I_{9/2} \rightarrow {}^2H_{9/2} \quad \text{spaced} \sim 12,200\text{cm}^{-1}$$

Thus, wavelength pumping of around 810nm, 980nm and 15000nm, in inverse order, are very susceptible to induce excited state absorption (ESA). Of course, the success to rise up to high energy levels depends on intensity of pumping, lifetime of

the respective levels, multiphonon relaxation and ion concentration. But not only ESA can be present, also energy transference between ions can take place due to implicated resonances.

In spite of $^4\text{I}_{13/2}$ Er having an absorption oscillator strength from 2 to 10 times higher than for $^4\text{I}_{11/2}$ and $^4\text{I}_{9/2}$, efficient pump light absorption for $^4\text{I}_{11/2}$ ESA can be achieved by adding Yb ions as codoped impurity. This is due to the favorable oscillator strength of $^2\text{F}_{5/2}$ Yb level.

1.3.11 Electronic configuration of Rare Earths

1.3.11.1 Motivation: Atoms of several electrons

In quantum mechanics, the simplest atomic system is the hydrogen atom H. In this case, the set of eigenstates with their respective eigenvalues of energy are obtained analytically by solving the Schrödinger equation. This procedure can be completed because the Hamiltonian is expressed in spherical coordinates and the variable separation is done in a straight way. Here, the energy values depend only on the principal quantum number n . This leads to degenerated states with different quantum numbers l , m and s . Anyway, eigenstates and energies are well established.

However, when more than one electron is implicated (i.e. all the other atoms), the electron repulsion term (see Equation 1.5) makes it impossible to get the analytic complete solution to the Schrödinger equation, so approximations and numerical solutions should be employed.

For the neutral atom of Z electrons, if the nuclear finite mass effect and the relativistic corrections are neglected, the Hamiltonian operator that describes the motion of the electrons is:

$$H = \sum_{i=1}^Z \frac{\vec{P}_i^2}{2m_e} - \sum_{i=1}^Z \frac{Ze^2}{R_i} + \sum_{i<j}^Z \frac{e^2}{|R_i - R_j|}, \quad (1.5)$$

where $e^2 = \frac{q^2}{4\pi\epsilon_0}$ and the first sum is the total kinetic energy of the system of Z electrons, the second one is the attraction exerted on each electron by the nucleus (potential field) and the third sum is due to mutual repulsion of the electrons (this sum has $(Z(Z-1)/2)$ terms).

1.3.11.2 Electron interaction

If the repulsion term is absent, the electrons will become independent. The Hamiltonian would be the sum of the hydrogenlike Hamiltonian of the electrons placed individually in the Coulomb potential $-Ze^2/r$.

Nevertheless, when the mutual interaction term can not be neglected, there are two approaches to deal with it: a) We make the additional term very small in order

to use the standard perturbation theory or b) Use density functional theory where the wavefunction that gives the minimal energy is sought out [27].

1.3.11.3 Central Field Approach

In the first approximation, the existence of further $Z - 1$ electrons affects a particular one since their charge distribution partially compensates the electrostatic attraction of the nucleus. Therefore, the i th-electron is considered to move in a potential which depends only on its position \vec{r}_i and takes into account the average effect of the repulsion of the other electrons by $V_c(r_i)$. This is the central potential of the atom.

Of course, this can only be one approach because the movement of the i th-electron actually affects the movements of the other electrons. Besides, when the i th-electron is close to the j th-electron, the repulsion that it exerts to the i th one, becomes so predominant that the potential will not be central. However, in quantum mechanics is possible to interpret the delocalization of the electron as if it distributed its charge over the whole space.

The perturbation theory can not be applied directly in Equation 1.5, because the third term is not small enough compared with the other terms. Therefore, the Hamiltonian is defined as:

$$H = \sum_{i=1}^Z \left(\frac{\vec{P}_i^2}{2m_e} + V_c(R_i) \right) + W, \quad (1.6)$$

where

$$W = - \sum_{i=1}^Z \frac{Ze^2}{R_i} + \sum_{i < j}^Z \frac{e^2}{|R_i - R_j|} - \sum_{i=1}^Z V_c(R_i),$$

here, it is possible to make W smaller in the hamiltonian $H = H_0 + W$ so W can be consider as a perturbation term.

The central potential $V_c(r)$ to which a given i th-electron is subject depends on the spatial distribution of the $Z - 1$ electrons, and this distribution, in turn, depends on the potential $V_c(r)$, since the wavefunction of the $Z - 1$ electrons must also be calculated from $V_c(r)$. Therefore, it is necessary to attain a coherent solution (so-called self-consistent) by which the wavefunction determined from $V_c(r)$ gives a charge distribution which reconstitutes this same potential $V_c(r)$.

1.3.11.4 Energy levels of the atom

From this behavior it is possible, at least qualitatively, to understand some important aspects as the relative position of the energy levels. For instance, at short interaction distance, the electron is inside the charge distribution of the other electrons sees

CHAPTER 1. ANTECEDENTS

1.3. RARE EARTHS GENERALITIES

only the attractive potential of the nucleus $V_c(r) \sim -Ze^2/r$. For the large distance, outside of the formed cloud by the $Z - 1$ electrons, the distribution can be treated globally so the electronic cloud covers the nucleus field. Therefore, the potential will be $V_c(r) \sim -e^2/r$. From those extremes, for intermediate values of r , $V_c(r)$ varies in a quite complicated way, but not as simple as $V_c(r) \sim 1/r$. As a consequence, the degeneracy energy states observed in the H atom will not be present anymore.

For the principal quantum number (n) fixed, the energy is lower when the corresponding eigenstate is more penetrating, this is, when the probability density of the electron in the vicinity of the nucleus is larger, then the screen effect is smaller. As it is known, as the orbital quantum number l increases, will be further localized the electron cloud of the nucleus. Therefore, the energies $E_{n,l}$ associated with the same value of n can be arranged in order to increase the angular momenta:

$$E_{n,0} < E_{n,1} < \dots < E_{n,l=n-1}.$$

Although for a given value of l , the energy $E_{n,l}$ still increases with n

$$E_{n,l} < E_{n',l}; \quad \text{if } n' > n.$$

As n increases, additional values of l arises and because the energy depends on both n and l , inversion order occurs, so there are states that appear in the expected inverse order for hydrogen states.

In the atomic ground state, inversions are originated because the external shell can contain only s and p electrons and then the subshells d and f are filled as inner subshells, this increases its energy. The first inversion is $4s, 3d$. Here, the $4s$ shell has a slightly lower energy than that of the $3d$ shell. This is explain since the $4s$ wavefunction is more penetrating that the $3d$ wavefunction. This demonstrates the importance of the inner-electron repulsion. One important example of this filling order inversion is the electronic constitution of the lanthanide group.

1.3.11.5 Spectral Terms for Lanthanides

The traditional spectral term notation is like the usual in the electronic configuration for atoms, except that here, uppercase letters are used as proposed by Russell and Saunders:

$$\begin{array}{cccccccccccccc} L= & 0 & 1 & 2 & 3 & 4 & 5 & 6 & 7 & 8 & 9 & 10 & 11 & 12 \\ & S & P & D & F & G & H & I & K & L & M & N & O & Q \end{array}$$

Where the capitals S, P, D, F, have to be omitted from the alphabetic sequence and if number L exceeds 20, it will be denoted by its value. Also, the letter J has been omitted.

CHAPTER 1. ANTECEDENTS

1.3. RARE EARTHS GENERALITIES

If the spin electron multiplicity is 1, it is named as a singlet term, when it is 2, this corresponds to a doublet term and so on. In the former case, in the case of two electrons contribution, they have antiparallel spin ($S = \frac{1}{2} - \frac{1}{2} = 0$) while in the triplet term, the two electrons have the orientation of their parallel spins ($S = \frac{1}{2} + \frac{1}{2} = 1$).

In the spectral term notation, within a given electronic configuration, there may be many possible term symbols. This is consequence of the different ways that the electrons can couple their angular momenta.

In closed shells (For instance, He : $1s^2$), there are not either total quantum orbital momentum ($L = 0$) or total spin momentum ($S = 0$). This two statements belong to Hund's laws [28]. For instance, the spectral term for He in its ground state is ($L = 0, S = 0$, spin multiplicity $2S + 1 = 1$) 1S .

For the case of lanthanides, the optical properties arise only from the $4f$ electrons configuration ($n = 4, l = 3$) and because these electrons are equivalent, they have to combine their other two quantum numbers (m_l, s) according to the Pauli principle. Then, the total allowed sum leads to the angular momentum L and the total spin S . Only three cases will be explained. For other configurations is recommended to consult Robert D Cowan's textbook [29]. The $4f^1$, $4f^2$, and $4f^3$ (Ce^{3+} , Pr^{3+} Nd^{3+} , respectively), will be examined.

The orbital L and spin S momenta coupled to give a total momenta. This spin-orbit coupling depends on the considered scheme. For example, in light atoms is costume to assume weak spin-orbit coupling, this is the so-called Russell Saunders coupling. Although, in heavy atoms this coupling is big and the scheme to handle is the jj coupling. But in lanthanides, the spin orbit interaction is of the order of electron repulsion. So an intermediate scheme coupling must be regarded. The general procedure to find the spectral terms that describe this coupling is: for given values of L and S , the total momentum J is given by

$$J = L + S, L + S - 1, \dots, |L - S| \quad (1.7)$$

1.3.11.6 Trivalent Cerium Spectral Terms

This is the most simple example where the single $4f$ electron gives place to the $L = 3 = F$ orbital momentum. The multiplicity of spin is two (up and down) and therefore the spectral term is 2F . But, according to Eq. 1.7, this gives $^2F_{7/2}$ and $^2F_{5/2}$ multiplets. Which of these multiplets are larger?. In this case, this question is answered by the Landé interval rule: $\Delta E = E_J - E_{J-1} = AJ$, where A is a constant. When A is positive, it is known as a normal multiplet, while if A is negative, it is known as an inverted multiplet. Although the behavior of the normal or inverted multiplet can vary from atom to atom, is useful to take for ground terms:

- If an orbital is partially filled with equivalent electrons and is less than half

full, the multiplet that arises is normal.

- If an orbital is partially filled with equivalent electrons and is more than half full, the multiplet that arises is inverted.

Therefore, in Ce is expected that the relative energy positions would be: $E(^2F_{5/2}) < E(^2F_{7/2})$.

One useful rule -regarding terms which arise from equivalent electrons- is that the vacancy in the orbital behaves (in respect of the terms which arise) like one electron.

1.3.11.6.1 Trivalent Ytterbium Spectral Terms As a consequence of that fact, because Yb^{3+} has $4f^{13}$ equivalent electrons (one vacancy), it can come up to with $^2F_{5/2}$ and $^2F_{7/2}$ multiplets, but it is expected to occur an inverted multiplet $E(^2F_{5/2}) > E(^2F_{7/2})$.

1.3.11.7 Trivalent Praseodymium Spectral Terms

In trivalent Praseodymium, two corresponding $4f$ electrons are responsible of the optical properties. When the antisymmetrization postulate is applied [30, 31], it gives as a constrain that $L + S = \text{even}$. From this condition, the spectral terms are found:

$$f^2 \rightarrow ^1S, ^3P, ^1D, ^3F, ^1G, ^3H, ^1I.$$

Now, which of these terms is the ground term?. Here, it is necessary to apply Hund's rules for comparable electrons: 1) From the arising terms, those with the highest multiplicity lie in the lowest energy level. 2) From these, the lowest is that with the highest value of L .

Thus, applying these rules, it is expected that 3H , be the ground term. As an example, from Eq. 1.7 ($L = 5 = H, S = 1, J = 6, 5, 4$) this triplet term is split into:

$$^3H \rightarrow ^3H_6, ^3H_5, ^3H_4,$$

and from this multiplet, according to the Landé interval rule, it is expected that the normal multiplet lead to $E(^3H_4) < E(^3H_5) < E(^3H_6)$.

If the vacancy rule is applied, also Thulium ($4f^{12}$, two vacancies) leads to the same spectral terms.

1.3.11.8 Trivalent Neodymium Spectral Terms

In trivalent Neodymium, three equivalent $4f$ electrons are responsible for the optical properties of the ion. The allowed spectral terms, in this case, are given by one more complicated rule for three equivalent electrons [22, 32]. It gives the terms:

$$f^3 \rightarrow {}^2(PD_2F_2G_2H_2IKL), {}^4(SDFGI),$$

from this, the highest multiplicity and value of L is 4I and this is the ground term. As an example, from Eq. 1.7 ($L = I = 6, S = 3/2, J = 15/2, 13/2, 11/2, 9/2$) 4I is split into:

$${}^4I \rightarrow {}^4I_{15/2}, {}^4I_{13/2}, {}^4I_{11/2}, {}^4I_{9/2},$$

and from these multiplets, according to the Landé interval rule, it is expected that a normal multiplet would lead to $E({}^4I_{9/2}) < E({}^4I_{11/2}) < E({}^4I_{13/2}) < E({}^4I_{15/2})$.

If the vacancy rule is applied, also Erbium would lead to the same spectral terms. Although, an inversion of the order is expected $E({}^4I_{9/2}) > E({}^4I_{11/2}) > E({}^4I_{13/2}) > E({}^4I_{15/2})$.

This work studies only Er and Yb ions, so just their spectral terms are shown. For other cases, it is recommended to consult references [21, 22, 32].

Final Comments

As it was seen, the research of light generation via upconversion plays an important role in both basic science and advanced applications. Study and characterization of diverse host materials that are candidates to carry active ions will continue in accordance to novel applications. This thesis is focused in the study of Erbium-Ytterbium doped barium zirconate and its luminescent characteristics. The Synthesis, structure, and morphology characterization of BZO was done at Instituto Mexicano del Petróleo (IMP) by Drs. Angeles-Chávez and Pedro Salas as a result of a long standing collaboration between the advanced materials group at CIO and the IMP. A brief resume of these results is presented in Chapter two. The study of the optical properties and emission performance of active ions within the BZO matrix under IR radiation was performed in the spectroscopy Laboratory at CIO. These results represent the core work of this thesis and are discussed in Chapter 3. The achieve visible emissions are explained qualitatively in accordance to the experimental data.

Chapter 2

Synthesis, Structure and Morphology of BZO

In this chapter we present the obtaining of barium zirconate nanocrystallites via low cost hydrothermal process. The crystalline phase of BZO is inquired by x-ray diffraction as well as how this varies with the annealing treatment and doping ion concentration. The nanoparticle morphology is analyzed from scanning electron microscopy and transmission electron microscopy. High resolution transmission electron microscopy is used to “see” how atoms are arranged and to confirm the x-ray diffractions results.

2.1 BaZrO₃ Nanocrystallites Synthesis

Although barium zirconate has been obtained by several processes [18, 33, 34] including physical methods such as mechanical milling, and inert gas condensation, along with chemical methods such as oxidative precipitation, electrodeposition, hydrothermal, and sol-gel synthesis, we use the hydrothermal process and it is described in the next section. In general, the principal advantage of the chemical methods is their relatively low-cost equipment.

Barium zirconate particles have been synthesized through solution-based methods with a variation of the particle size that ranges from microns to nanometers of the crystal [35, 36, 37]. In BZO nanoparticles, the solution precipitation and hydrothermal synthesis has been successful in producing amorphous nanoparticles. Upon heat treatment they can grow as either micro-sized particles or nanocrystalline agglomerations of micron scale particles.

2.1.1 Hydrothermal Process

The $\text{Yb}_2\text{O}_3 - \text{Er}_2\text{O}_3$ codoped BaZrO_3 nanoparticles with 2 mol % Yb_2O_3 , 1 mol % Er_2O_3 and single doped 2 mol %. Yb_2O_3 , and 1 mol% Er_2O_3 nanoparticles were obtained by hydrothermal process *. All reagents were analytically pure and used without further purification. Barium nitrate ($\text{Ba}(\text{NO}_3)_2$), zirconyl chloride octahydrate ($\text{ZrOCl}_2 \cdot 8\text{H}_2\text{O}$), erbium nitrate ($\text{Er}(\text{NO}_3)_3 \cdot 5\text{H}_2\text{O}$) and ytterbium nitrate ($\text{Yb}(\text{NO}_3)_3 \cdot 5\text{H}_2\text{O}$) were used as the predecessor materials for the $\text{Yb}^{3+} - \text{Er}^{3+}$ codoped barium zirconate nanoparticles. Sodium hydroxide (NaOH) was used as the precipitating agent. Cetyltrimethylammonium bromide (CTAB, $\text{CH}_3(\text{CH}_2)_{15}\text{N}(\text{CH}_3)_3\text{Br}$) was the surfactant and ethanol was the cosurfactant.

In a typical procedure, see Fig. 2.1, barium nitrate (4.53g), zirconyl chloride (5.58g), erbium nitrate (0.16g), ytterbium nitrate (0.32g) and CTAB (cetyltrimethylammonium bromide) (1.9g) were dissolved in a solution of ethanol-water ($\text{CH}_3\text{CH}_2\text{OH}$, H_2O) at room temperature applying vigorous stirring for 1 h. Under strong stirring, sodium hydroxide was added and stirred again for 1h at room temperature. The hydrothermal reactions were carried out in a Teflon bottle (500 ml in total capacity) under autogenous pressure at 100 °C for 24h. The precipitate was then washed with distilled water and dried in an oven at 100 °C for 15h. Lately, it was annealed at 500 °C or 1000 °C for 3h, with a heating rate of 3 °C/min.

2.2 Structure and Morphology

To evaluate the physical aspects of the atomic arrangement of nanocrystalline samples, it is necessary to use techniques capable of measuring quantities on the range of 1Å. There are some options, for instance, if a short wavelength probe is investigated, we have to consider an X-Ray emission whose wavelength range is around 1Å. In this nanometric scale, no visible light ($5 \times 10^3 \text{Å}$) can be employed. Because we have to inquire how the atoms are arranged and the type of crystalline structure that we are studying.

2.2.1 X-Ray Diffraction

In 1912, Max von Laue suggested that the arrangement of the atoms in crystalline solids, in which the (this was believed without a direct proof, just based on the cut-edge face micrography) that followed a regular pattern, might be used as diffraction gratings for measuring x-ray wavelengths.

*Notation for the samples concentration will be referred as BZO:Yb(2%), BZO:Er(1%), and BZO:Yb(2%),Er(1%), for BZO: 2 mol % Yb_2O_3 , 1 mol % Er_2O_3 , and 2 mol % Yb_2O_3 , 1 mol % Er_2O_3 , respectively

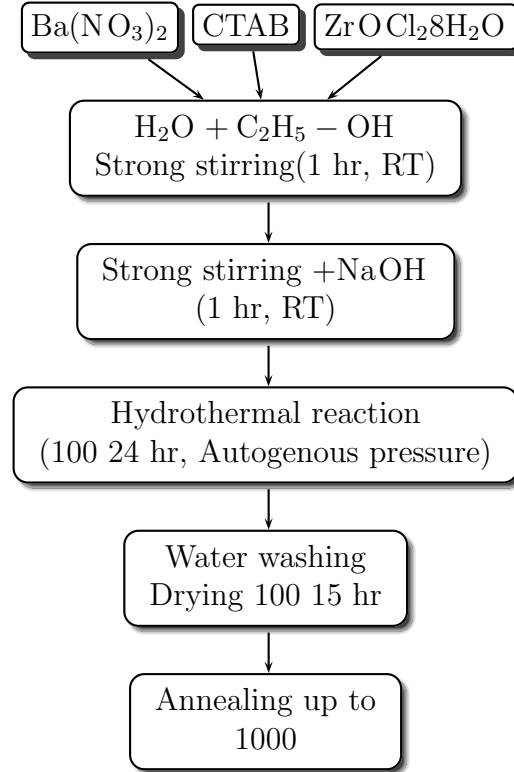


Figure 2.1: Hydrothermal synthesis process to obtain BZO nanocrystalline.

When a wave-probe impinges upon a collection of scattering centers, each scattering center generates waves that are radiated outward, in all directions. The resultant wave in one specific direction depends on the interference between all the separate centers. It is a remarkable fact that the atoms lying on any plane within the crystal, act with respect to the incident wave as a semimirror concerning to visible light; that is, they reflect a portion of the wave whereas allows the rest to pass through. These are the Bragg planes and Bragg reflections that in 1913 W. H. Bragg and W. L. Bragg (father and son, respectively) used to develop the fundamental theory of x-ray diffraction by crystals.

In a crystalline arrangement, if an incident wave at a θ angle hits Bragg parallel planes (not the normal to the reflecting planes), the wave is partially reflected at an angle θ from the Bragg planes. If the reflection of the second plane is taken into account, the two reflected waves will constructively interfere at any distant point, only if they are in phase. The condition for constructive interference between waves reflected from adjacent parallel Bragg planes, which are separated by an interplanar

CHAPTER 2. SYNTHESIS, STRUCTURE AND MORPHOLOGY OF BZO

2.2. STRUCTURE AND MORPHOLOGY

distance d , is:

$$n\lambda = 2d \sin \theta, \quad (2.1)$$

where the order of the reflection n takes positive integer values, λ is the wavelength of the incident x-ray. This equation is known as the Bragg's law and is the basis of all coherent x-ray and electron diffraction effect in crystals (De Broglie waves). It is used to measure interatomic distances comparable to wavelength. For instance, if n , λ and θ are known, d can be computed. The angle between the undeviate ray and the reflected ray is 2θ and the Bragg planes are parallel to the bisectrix of this 2θ angle.

An X-ray diffractometer is used to measure interatomic distances and to identify reflection planes. A monochromatic x-ray source impinges on a crystal sample whose structure and interatomic dimensions are unknown. A detector that is sensitive to x-ray ionization effects gets the intensity of the x-rays. Even though the detector and the sample can be rotated, the detector is set at angle 2θ from the forward beam, as is shown in Fig 2.2. The x-ray intensity in the detector indicates a strong maximum when the Bragg condition is satisfied. Thus, it is possible to determine d .

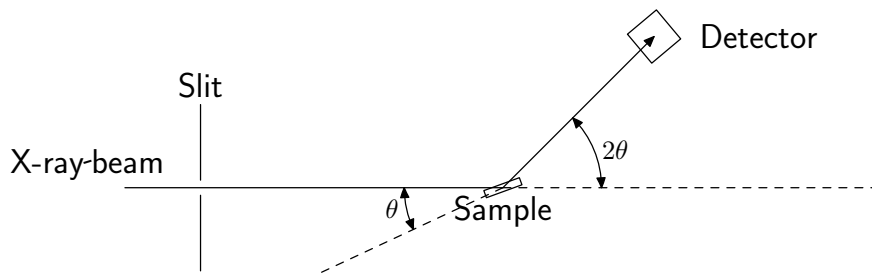


Figure 2.2: Schematic representation of an x-ray diffractometer

If the sample used is powder, it consists on a very large number of randomly oriented nanocrystallites. Only those particular nanocrystallites that are oriented in such way as to satisfy the Bragg condition, will produce a strongly diffracted beam (see Fig. 2.3). The other nanocrystals will not diffract the incident beam coherently. Therefore, the emerging beam will consist of two parts: an intense, central undeviated beam and a scattered beam that makes a 2θ angle with respect to the incident beam. The θ angle is uniquely determined, for a given order, by the Bragg relation.

When the scattered beam is detected in one plane, an intensity pattern consisting of a strong central spot surrounded by a circle is used -by measuring its radii and the distance between the sample and the plane- to determine the 2θ angle and thus the interplanar distance can be calculated from the Bragg relationship.

Actually, there are many sets of planes in any single crystal. A Bragg plane is any

**CHAPTER 2. SYNTHESIS, STRUCTURE AND MORPHOLOGY
OF BZO**

2.2. STRUCTURE AND MORPHOLOGY

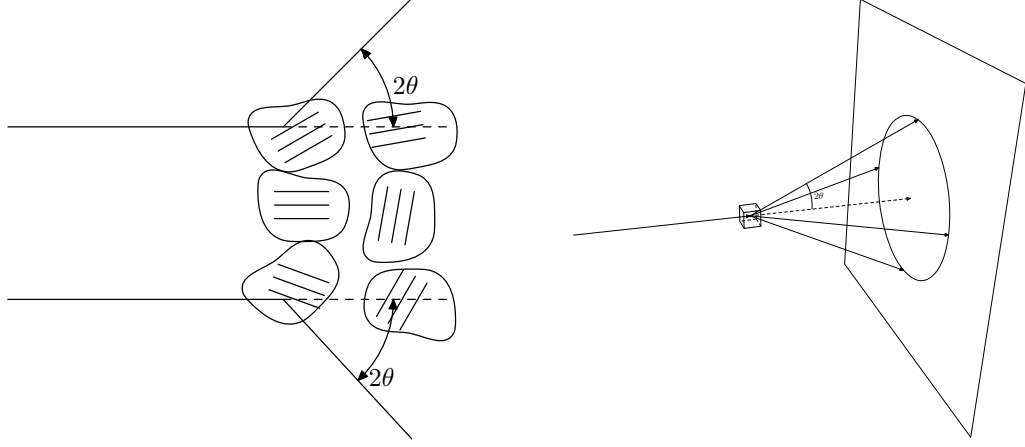


Figure 2.3: Right, Nanopowder crystallites are scattering the incident x-ray radiation. The ones that satisfy with the Bragg condition will interfere constructively and will form a circular pattern.

plane that contains atoms. So many planes can be defined. It is clear, that the various planes will differ in the values of their interatomic space d , consequently, there will be a number of Bragg angles θ , that satisfy the Bragg relation for a particular set of Bragg planes. The x-ray diffraction pattern will therefore be somehow more complicated than the indicated in Fig. 2.3. It will have a number of concentric circles (called Debye and Scherrer rings). Each one corresponds to a diffraction from a particular set of Bragg planes. The intensities of the reflected beams from the different planes will not be the same, because both the number of atoms per unit area in one plane and the type of atoms, may differ from it in another plane. The effectiveness of an atom to scatter radiation is due to both the number and the distribution of electrons in the atom [38]. So, if different atoms form the lattice, different intensities peaks are expected. This characteristic is taken into account by the atomic form factor f .

When N atoms are in the base associated with one lattice point, the scattering radiation from these atoms may interfere constructively or destructively depending on the position of the atoms. The arrangement of the atom and their individual atomic form factors are included in the structure factor $S_{h,k,l}$ [39].

$$S_{h,k,l} = \sum_{j=1}^N f_j e^{-i(kx+ly+mz)}, \quad (2.2)$$

here x , y , and z are the coordinates of the j th-atom as fractions of the lattice constants. The exponential factor explains the difference in phase of the scattered waves due to their path difference, as they scatter from atoms at different positions in the crystal. Thus, the intensity of the scattered X-Ray is proportional to $|S_{h,k,l}|^2$.

CHAPTER 2. SYNTHESIS, STRUCTURE AND MORPHOLOGY OF BZO

2.2. STRUCTURE AND MORPHOLOGY

2.2.1.1 XRD Measurement

In order to investigate the crystalline structure and the crystallite size of the samples, X-Ray Diffraction was obtained with a SIEMENS D-500 diffractometer equipment provided with a Cu-Ktube with α radiation at 1.5426 Å, scanning in the interval from 20° to 70° 2θ with increments of 0.02° and swept time of 8 s.

2.2.1.2 XRD Results and Discussion

X-ray diffraction patterns of as synthesized as well as 1000 °C and 500 °C annealed BZO samples were obtained. In this part, just for clarity, only the XRD of 1000 °C annealed BZO nanopowder samples are shown in Fig. 2.4. This is done due to the great similarity among XRD patterns. They are shown in appendix B. The main characteristic peaks (30.13°, 37.12°, 43.12°, 53.5°, 62.44°) are indexed in correspondence with 6-0399 standard JCPDS for pure cubic perovskite BaZrO₃ with a lattice constant of 4.18Å. As the annealing temperature increases, crystallinity enhances, as is suggested by the increasing intensity of the main reflection of the plane [1 1 0] as temperature increases from 100°C to 1000°C. If the diffraction pattern of the Er – Yb codoped BaZrO₃ is compared with an undoped sample at the same temperature, we do not observe measurable changes. This confirms the high structural stability of the cubic perovskite phase for doping concentrations as high as 3% mol Rare Earth ions.

If the Scherrer's equation is applied in order to estimate the average crystallite size as:

$$D = \frac{0.9\lambda}{\Delta B \cos \theta}, \quad (2.3)$$

where ΔB is the full width at half maximum diffraction peak, λ is de X-ray wavelength and θ is the position of the strongest diffraction peak. The average particle size thus found is:

Annealing	100 °C	500 °C	1000 °C
Particle size(nm)	51.3	64.5	70.4

Table 2.1: Particle size as annealing temperature is increased.

From these results, it is observed (Table 2.1) that the estimated particle size grows as the annealing temperature increases as a consequence of the coalescence between particles.[†]

[†]These are the estimations of the primary particles or crystallites that XRD see independently of its aggregation in bigger secondary particles [40].

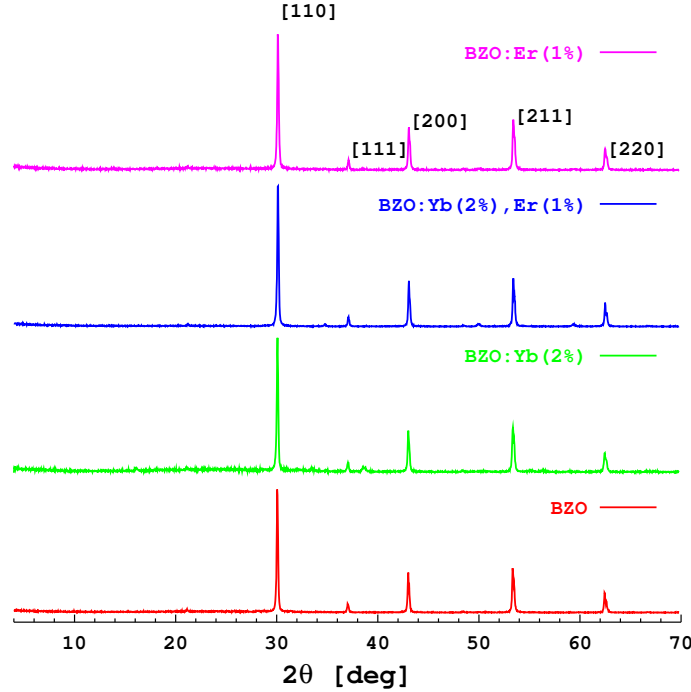


Figure 2.4: X-Ray Diffraction patterns of BaZrO_3 annealed at 1000°C . The upper patterns correspond to doped and codoped samples whereas the pattern at the bottom corresponds to undoped samples.

2.2.2 SEM, TEM and HRTEM

When it is desirable to know the physical aspect (morphology) of one object within the vision scope, imaging systems should be employed. However, the all real system has intrinsic limitations. For instance, in typical optical microscopy, the image of one small sample can be amplified 1500x with a resolution of $0.2\mu\text{m}$, but diffraction limit is insuperable. With the purpose of small wavelength, electronic microscopy has been used in accordance with De Broglie postulate. As in optical microscopies the glass lenses bend the light, in electronic microscopy the electrons beam is bend by magnetic fields.

2.2.2.1 Scanning Electron Microscope

In Scanning Electron Microscopy (SEM), electrons are generated from thermionic or field emission cathode and accelerated by a voltage of 1-50 kV between cathode to anode. The electron probe diameter is around 1-10 nm with probe current of 10^{-10} - 10^{-12}A and impinges over the specimen surface. This focussing is achieved by a pair of electromagnets acting as condenser lenses. A deflection coil system in front

CHAPTER 2. SYNTHESIS, STRUCTURE AND MORPHOLOGY OF BZO

2.2. STRUCTURE AND MORPHOLOGY

of the objective lenses scans the electron probe in a raster across the specimen and in synchronism with the electron beam of a separate cathode-ray tube (CRT). The intensity of the CRT is modulated by one of the signals recorded to form an image. The magnification can be increased simply by decreasing the scan-coil current and keeping the image size of the CRT constant [41].

When the primary electrons collide with the sample, they lose energy by repeated scattering and absorption within the sample. This interaction between the electron beam and the sample results in the emission of electrons and electromagnetic radiation which can be detected to produce an image by the secondary electrons (see Fig. 2.5). These electrons have energy around 2-5eV. By convention, the limit between secondary electrons and backscattered electrons is 50eV. Secondary electrons are generated by inelastic excitation to high energy levels so the excited electrons can overcome the work function before being decelerated to the Fermi level. Backscattered electrons are between 50eV and the accelerator potential energy $E = eU$. This range is due to deceleration of electrons that have suffered multiple energy losses and multiple scattering through large angles. Auger electron production is an alternative to characteristic x-ray emission after the ionization of an inner shell. The de-excitation energy released when an electron from an upper shell fills the vacancy in the ionized shell can be converted to an x-ray radiation or the energy may be transferred to another atomic electron, which leaves the specimen as an Auger electron.

If the specimen is transparent to the incident electrons, the transmitted electrons can easily be recorded by a scintillation or semiconductor detector situated below the specimen support. A sample that shows sufficiently transmission to 10-50KeV electrons will be an excellent specimen for a 100 keV Transmission electron microscopy (TEM). The recording of transmitted electrons is an additional possibility in SEM.

Secondary electrons are generated within a few nanometers from the sample surface and then they can be detected by using a photomultiplier device and the resulting signal can be put into a two-dimensional array as a digital image or be displayed as already was mentioned. The brightness of the signal is proportional to the number of secondary electrons picked by the detector. When one uniform area is activated, certain number of electrons are emitted from this surface zone. But when this area is nonuniform about the axe beam (oblique incidence), one side of the beam will decrease and more secondary electrons will be detected. Then, edges are brighter than flat surface. This leads to images with three-dimensional appearance. By using SEM a resolution of 1nm can be achieved. However, the imaging of a surface topography by Transmission electron microscope (TEM) is superior by one order of magnitude in resolution [41].

CHAPTER 2. SYNTHESIS, STRUCTURE AND MORPHOLOGY OF BZO

2.2. STRUCTURE AND MORPHOLOGY

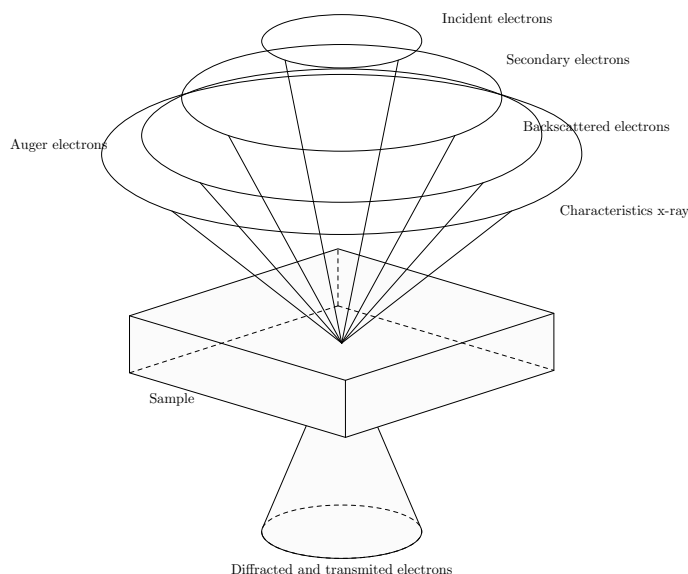


Figure 2.5: Electron beam is incident in the sample, then electrons go under one of the depicted processes.

2.2.2.1.1 Sample preparation for SEM In order to get a minimal scattering from the environment, a vacuum is conventionally made. So, moist samples will produce vapor and need to be degassed. This implies that transition liquid-gas phase could not be observed. However, with the technological advance, it is possible to observe samples in low-pressure gaseous environments (10-50 Torr) and high humidity (up to 100%). This can be done by the development of a secondary electron beam capable of operating in presence of water vapor.

2.2.2.2 Transmission Electron Microscopy

Transmission Electron Microscopy (TEM) is also an image formation technique that is very similar to SEM imaging. The main difference is that, while in the last secondary electrons are detected, in the former transmitted electrons that cross the sample are used. Then an image is formed and enlarged, and can be displayed on a fluorescent phosphor screen or saved into a photographic film. Some structural details in the sample can be improved by depositing a thin film of heavy atoms on the sample. This is done owed to the fact that dense nuclei of the heavy atoms scatter the electrons out of the beam. The electrons that remain in the beam can be detected as it was pointed out. Areas where electrons are scattered appear darker on the display.

In spite of its advantages, the TEM technique has a number of drawbacks. Mate-

CHAPTER 2. SYNTHESIS, STRUCTURE AND MORPHOLOGY OF BZO

2.2. STRUCTURE AND MORPHOLOGY

materials require exhaustive sample preparation to have thin samples that are transparent to electron beam. Also, the structure of the sample may change during the preparation. The relative small field of view could lead to the possibility that the region inspected may not be characteristic of the whole sample. Special care should be put in biological samples since the electron beam can damage the material.

2.2.2.3 High-Resolution Transmission Electron Microscopy

High-Resolution Transmission Electron Microscopy allows the image formation of the crystallographic structure of a sample. This high resolution lets study nanoscale properties of the crystalline material. The resolution involved is around 0.8\AA . In this range, individual atoms are imaged.

Technical image formation for HRTEM does not include amplitude of the electron wave (absorption of the sample) for imaging. This is accomplished by the interference in the image plane of the electron wave with itself. Amplitude is measured as phase information can not be handled directly. But we have to recall that phase gives us the information about the sample and generates contrast in the image. This is why it is called phase-contrast imaging. However, the sample should be thin enough so the information of amplitude variations are not present in the image.

Interaction of the crystallographic structure within the sample can be understood as if wavefronts of the electron wave are plane. As it passes through the thin sample, it is attracted by the positive cores and conducted along the atoms columns of the lattice. As it was mentioned in Sec. 2.2.1, also the interaction between the electron wave in different atom columns leads to Bragg diffraction.

Postprocessing the electron wave, interference has to be done in order to get the actual phase and the image of the atomic arrangement. This can be done by either the holography method or through the focal series method.

2.2.2.4 SEM, TEM and HRTEM Procedure

Scanning Electron Microscopy (SEM) and Chemical analysis by Energy Dispersive X-ray Spectroscopy (EDXS, these results are presented in appendix C.) was performed in an environmental scanning electron microscope XL30 which has attached the X-ray energy dispersive spectroscope.

Transmission electron microscopy (TEM) images as well as high resolution transmission electron microscopy (HRTEM) were performed in a Tecnai G2 F30 S-Twin transmission electron microscope operating at 300 kV. The microscope is equipped with a Schottky-type field emission gun and an S-Twin objective lens ($C_s=1.2\text{mm}$; $C_c=1.4\text{mm}$; point to point resolution, 0.20 nm). Powder samples were suspended in isopropanol at room temperature and dispersed with ultrasonic stirring, and then the aliquots of the solution were dropped on 3 mm diameter lacey carbon copper grids.

CHAPTER 2. SYNTHESIS, STRUCTURE AND MORPHOLOGY OF BZO

2.2. STRUCTURE AND MORPHOLOGY

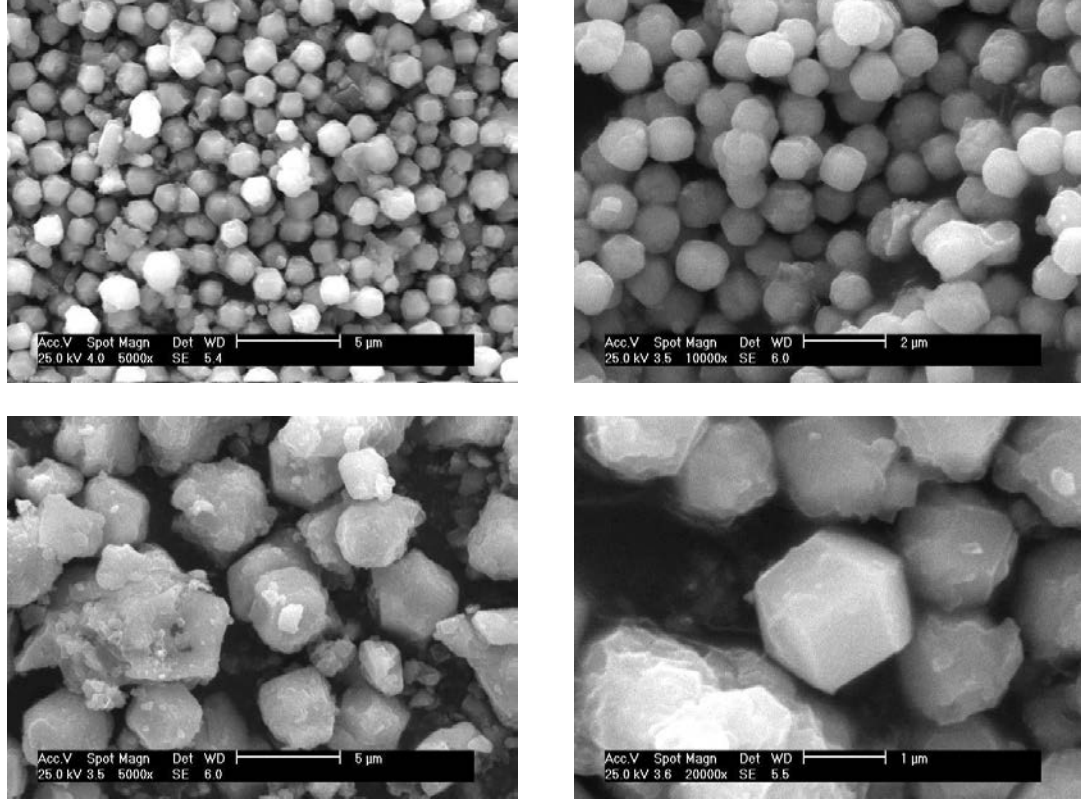


Figure 2.6: SEM images of codoped BaZrO_3 annealing at 500°C ; on the left upper corner: Er(1%) doped, on the left bottom corner: Yb(2%) doped, on the right upper corner: Yb(2%) – Er(1%) codoped and on the right bottom corner: Er(1%) doped (Zoom).

2.2.2.5 SEM, TEM and HRTEM results and discussion

SEM images of barium zirconate were obtained and are shown in Figs. 2.6. The images obtained depict, BZO secondary particles of submicron size. In spite that they are composed by several primary particles, cubic morphology and well defined crystallites were observed. This morphology feature is applicable to most of the particles observed. From Figs. 2.6, it is possible to obtain the distribution size showed in Fig. 2.7. 730nm is the average size of the secondary particles.

Images of crystallites obtained after annealing at 1000°C were observed by TEM and are shown in Figures 2.8. It is important to point out that well faceted individual cubic nanocrystals with average sizes around 125 nm are observed from TEM images. As an example, the size distribution for particles is taken from Figures 2.8 and it is shown in Figure 2.9. A HRTEM confirm the cubic perovskite lattice for one crystallite oriented with its $[011]$ direction perpendicular to the image or in parallel with the electron beam (Fig. 2.10). There, one can observe the almost undistorted

CHAPTER 2. SYNTHESIS, STRUCTURE AND MORPHOLOGY OF BZO

2.2. STRUCTURE AND MORPHOLOGY

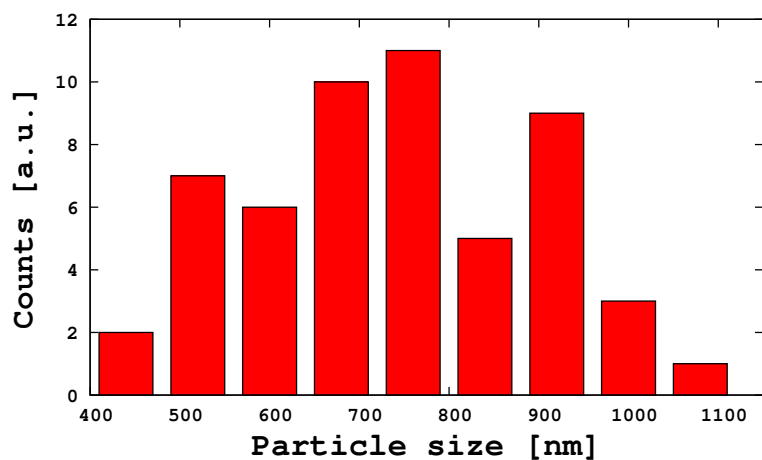


Figure 2.7: Distribution particle size of BZO 500 °C. The counts were taken from SEM images (Fig. 2.6). The average size is 730 nm.

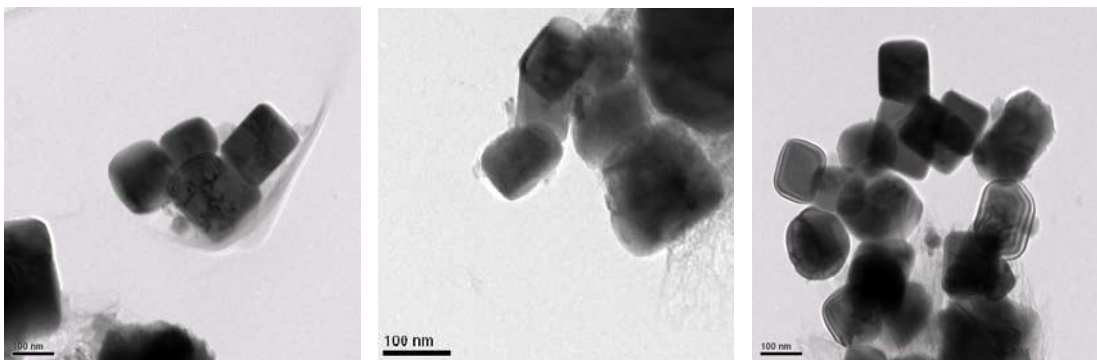


Figure 2.8: Three TEM images of BaZrO₃ annealed at 1000 °C.

cubic lattice that is confirmed by the Fast Fourier Transform (FFT) image showing the main diffraction points for such orientation (Fig. 2.10, right).

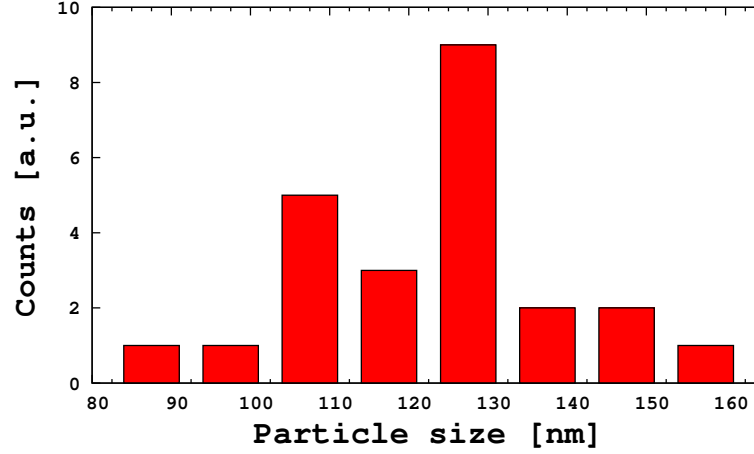


Figure 2.9: Distribution particle size of BZO 1000 °C. The counts were taken from TEM images (Fig. 2.8).

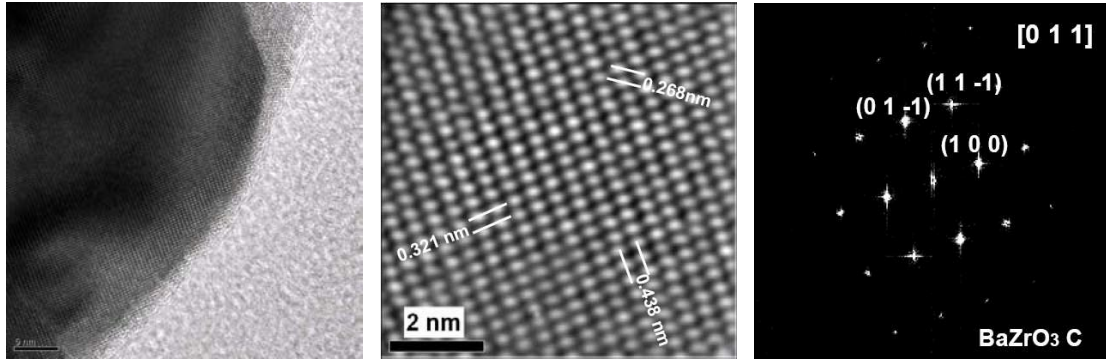


Figure 2.10: HRTEM images of BaZrO₃ annealed at 1000 °C (left), HRTEM zoom and labeling of lattice constants for a crystal-lite oriented with its [011] direction normal to the image (center), and Fourier transform of HRTEM, the principal reflections are indicated (right)

2.3 Infra-Red Fourier Spectroscopy

In order to know the phonon spectrum, Fourier transform spectroscopy was made by means of the Perkin Elmer Spectrum BX FT-IR System in the range of 350 to 1000 cm⁻¹.

Figure 2.11 illustrate the infrared absorption spectra of BZO. In this figure an important peak around 570 cm⁻¹ corresponds to the maximum phonon energy already reported for other Ca and Sr perovskites [42]. Although it peaks at 580cm⁻¹, the band is broad ($\sim 200\text{cm}^{-1}$). Another peak which is in 365cm⁻¹ is also due to

CHAPTER 2. SYNTHESIS, STRUCTURE AND MORPHOLOGY OF BZO

2.3. INFRA-RED FOURIER SPECTROSCOPY

the next eigenvalue of phonon energy. Another peak in 870 nm ((b) Fig. 2.11) is exclusive of BZO: Yb and is due to the broadening of $^4I_{13/2}$ ground level of Yb [43, 44].

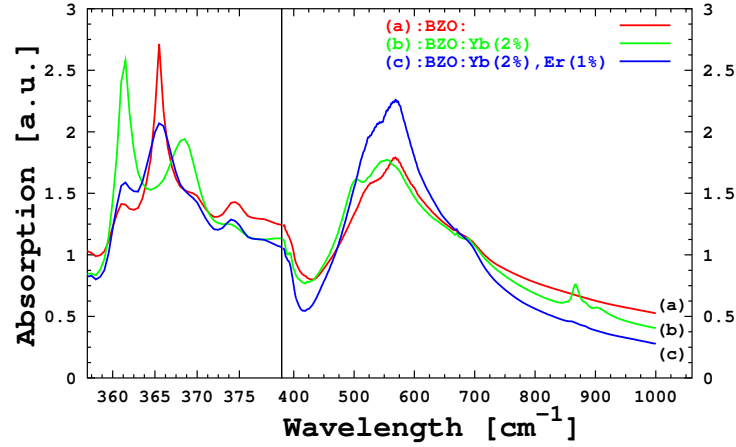


Figure 2.11: Infrared absorption spectra of a) BZO, b) BZO:Yb and c) BZO:Yb, Er.

Final Comments

Undoped, Er – Yb doped, and Er – Yb codoped barium zirconate were obtained by low-cost hydrothermal synthesis. This process has demonstrated strong reliability in the sense that no other segregation or crystal phase were observed under XRD analysis. Patterns found are uniquely of cubic phase in spite of rare earth doped concentration. The morphology of BZO particles as synthesized can be observed via SEM and TEM. In those, well faceted cubic crystallites were observed. HRTEM were used to confirm the cubic perovskite crystalline phase observed in XRD and interstitial spaces were indicated. If additional filtering is ejected in the samples, more monosized distribution should be expected.

Chapter 3

Optical Spectroscopy

3.1 Absorption Spectroscopy

In optical absorption spectroscopy, electromagnetic radiation in the near ultraviolet, visible, and near infrared ranges are used to excite the transitions between the electronic states of the sample under consideration. Experimental results are presented as plots of absorbed intensity versus photon energy ($E = h\nu$), frequency ν or wavelength (λ). When the sample consists on dispersed atoms, it is a low pressure gas and it presents very sharp lines. Although if the sample is a solid, we can observe different bandshapes. In general, the absorption intensity is related with the photon wavelength. Traditional notation for the abscissa coordinate can be energy units E (eV is used for optical photon), in wavenumbers $\bar{\nu}$ (the reciprocal is the wavelength in cm^{-1}), in frequency units (ν or ω) or wavelength (in nanometers (nm) or micrometers (μm)). Relations between these quantities are: $1\text{cm}^{-1} = 1.24 \times 10^{-4}\text{eV}$; $1\text{eV}=8066\text{cm}^{-1}$; and $E(\text{eV}) = 1.24/\lambda(\mu\text{m})$.

Frequently, the spectrometer output is given in terms of the specimen transmission, $T = I(\nu)/I_0(\nu)$ expressed as a percentage, or the optical density (also referred as absorbance), $OD = \log_{10}(1/T)$, that is related to the absorption coefficient $\alpha(\nu)$ according to

$$OD = \frac{\alpha(\nu)l}{2.303}. \quad (3.1)$$

Agreeing with Lambert's law, the attenuation of the incident radiation $I_0(\nu)$ to the sample of thickness l is given by

$$I(\nu) = I_0(\nu) \exp(-\alpha(\nu)l). \quad (3.2)$$

In practice $I_0(\nu)$ and $I(\nu)$ are measured and the value of an absorbing coefficient

$\alpha(\nu)$ at particular frequency is obtained using

$$\alpha(\nu) = \frac{1}{l} \ln\left(\frac{I_0(\nu)}{I(\nu)}\right). \quad (3.3)$$

3.1.1 Absorption Spectroscopy Procedure

The optical absorption spectra was obtained with a Perkin-Elmer UV-Vis-NIR Lambda 900 spectrophotometer using a 1 inch integrating sphere from Labsphere Co. The measured wavelength range goes from 200 nm to 2000 nm. Since the samples are powder, a reflection spectra directly obtained was converted into absorption spectra using an spectrophotometer software.

3.1.2 Absorption Spectroscopy Results

The absorption spectra of the BaZrO₃ samples annealed at 1000 °C are shown in Fig. 3.1. All samples in the 200 to 320 nm range, depict the particular UV edge of the BaZrO₃ host with a main peak at 239nm corresponding to 5.18eV band gap of BaZrO₃. The band gap does not change position with the substitution of up to 3% mol of RE ions within the crystalline lattice. The fact is in agreement with the XRD results in the sense that even though the high concentration of substituted RE ions is presented, the lattice does not show measurable changes in the structure and symmetry from the undoped crystalline phase.

The undoped BaZrO₃ spectrum shows that it is a very transparent material in the visible region up to 1650 nm, see Fig. 3.1. The only observable feature is a central peak at 1382 nm indicating the possible presence of residual H₂O and OH that remains within the BaZrO₃ crystallites. This peak also appears in the doped samples spectra suggesting that it is a consequence of the synthesis method.

Several ground states absorptions are identified in Fig. 3.1. As it is expected, the main difference between them is found the range between 800 to 1000nm where Yb has its well known absorption band (corresponding to ²F_{5/2} multiplets) in (b), but it is superposed with the ⁴I_{11/2} absorption of Er ion in (d) of the Fig. 3.1 where it can be seen that the absorption band of Yb – Er codoped sample is at least ten times bigger than that of Er doped sample (curve (c) in Fig. 3.1). This is an indication of the potential possibilities that Yb can to act as a sensitizer of Er.

In order to look for the effects of the annealing treatment, in Figure 3.2 is shown the absorption spectra of pure BZO for both 100 °C and 1000 °C annealing treatments. The significant reduction of the 1450 nm band is due to the annealing process since this band corresponds to OH radicals and becomes strongly reduced when is subjected to the annealing process at 100 °C and 1000 °C (from (b) to (a) in Fig.

CHAPTER 3. OPTICAL SPECTROSCOPY

3.1. ABSORPTION SPECTROSCOPY

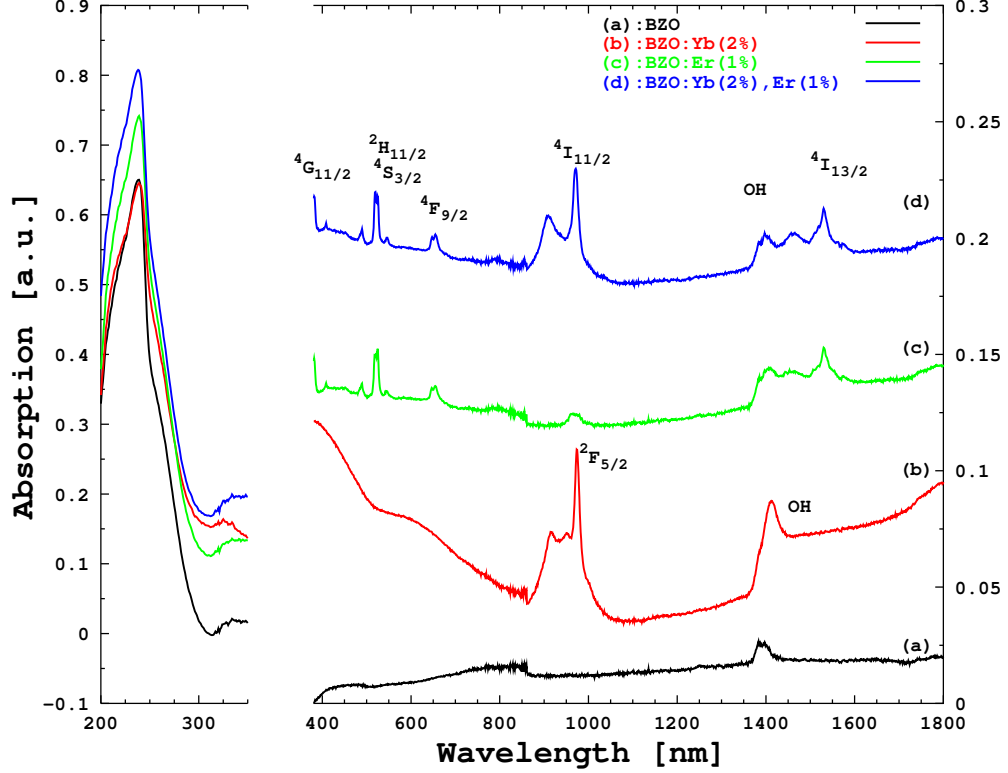


Figure 3.1: Absorption spectra of (a) BZO, (b) BZO:Yb, (c) BZO:Er, (d) BZO:Yb-Er, for samples annealed at 1000 °C.

3.2, respectively) *. Also, both the width of the peak due to BZO matrix and the right profile changes in accordance to annealed temperature.

In the left part of Fig. 3.2, there are two local maximums in BZO annealed 100 °C, the common peak at 239 nm and a secondary peak nearly to 300 nm. Thus, the single-peak is divided into two local maxima and its width is reduced. This variation can be attributed to a superficial ending of nanocrystals as BaO or ZrO₂ [45], see appendix A. The annealing of the samples seem to avoid the [1 0 0] terminal since the typical UV edge of ZrO₂ is nearly of 300 nm. However, a more detailed discussion and experimental support must be given to confirm this behavior.

Also the 1400 nm band is reduced in a significative way as the annealing temperature increases (right part of Fig. 3.2 from (a) to (b).)

It is important to notice that for the absorption spectra of Yb doped samples (see Fig. 3.3), there is a similar trend. The typical BaZrO₃ right lateral side of the band at 300nm goes to a small red-shift displacement and shows broadening as

*This is a typical overtone of the hydroxyl absorption nearly at 1400 nm.

CHAPTER 3. OPTICAL SPECTROSCOPY

3.1. ABSORPTION SPECTROSCOPY

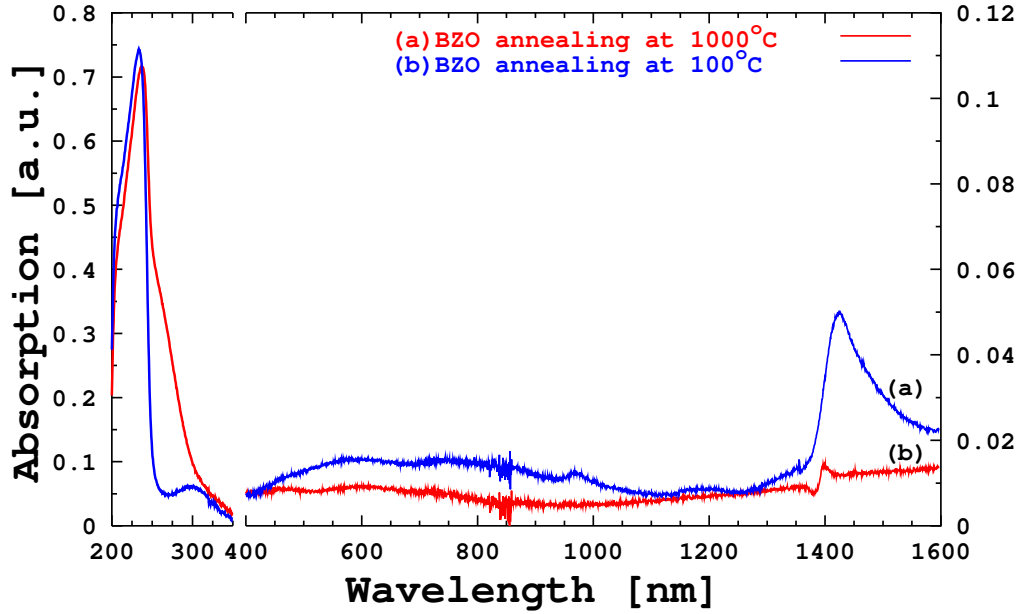


Figure 3.2: Absorption spectra of (a) BaZrO₃ annealed at 1000 °C and (c) BaZrO₃ without annealing

the annealed temperature is increased. That might indicate slight lattice distortions that are below the XRD sensitivity. In the left part of the Fig. 3.3, it is very clear how the secondary maximum is risen when the annealing temperature goes from 1000 °C to 100 °C (sequence (a)-(b)-(c) in Fig. 3.3).

Again, the 1400 nm band is reduced in a significative way as annealing temperature increases (right part of Fig.3.3,(c)-(b)-(a)), indicating again reduction of OH-radicals on the surface of the BZO crystallites. This fact is very important, as it will be discussed, to the dynamics of the non radiative process involving the OH impurities and RE ions, and the quenching process.

In the absorption spectroscopy results, it was never found the presence of other rare earth impurities. This fact is interesting since the RE elements, in spite of the high purity precursor employed (99.99%), are indeed chemically related, it is difficult to separate them from each other. So, impurities of other RE are inevitable

Relative positions of absorption peaks were used to obtain a classical Dieke diagram as is shown below (Fig 3.4). This was done in order to get and accommodate the relative positions of energy level of Er and Yb ions. It is realized in order to explain the possible energy transfer mechanism between Er – Er and Er – Yb ions.

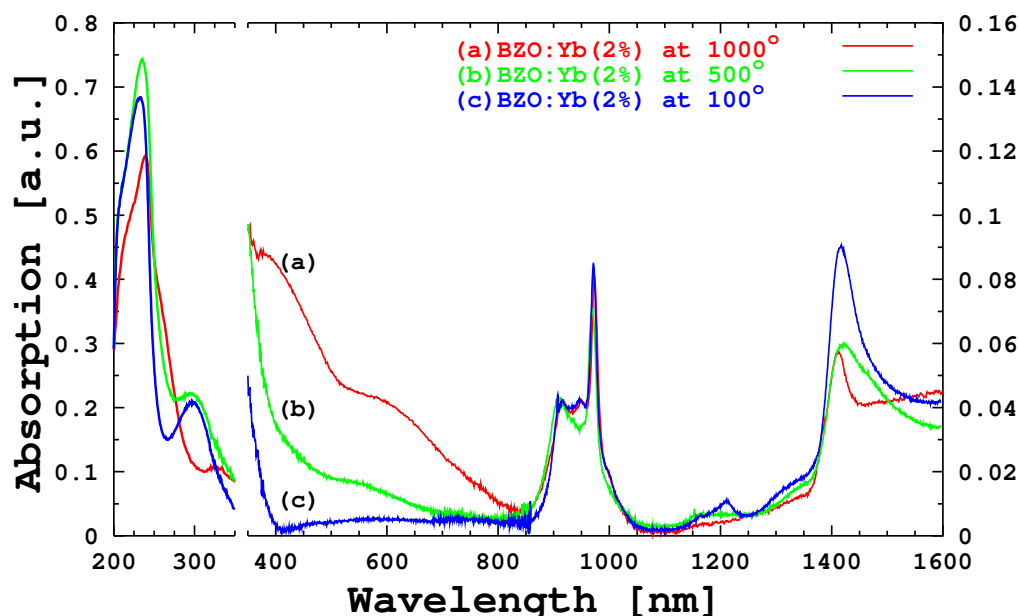


Figure 3.3: Absorption spectra of BaZrO₃ annealed at 1000°C, 500°C, 100°C

3.2 Emission Spectroscopy

Typical luminescence analysis is usually made by optical pumping using high intensity sources into strong absorption bands in the near ultraviolet and blue regions of the electromagnetic spectrum. Classical light sources are mercury and xenon lamps. Also, lasers may be used including Ar⁺, Kr⁺, He – Ne, and He – Cd lasers that have emissions at fixed wavelengths (down conversion). The light emitted by the sample may be resolved into its component bands using a prism or reflection grating monochromator. The light emerging from the monochromator is detected by an electron multiplier phototube with associated high voltage power supplies. Gallium arsenide phototube is particularly used in the visible range (280-900nm). In the near infrared range a lead sulphide cell, cooled germanium photodetector, or special III-V compound photodiode can be used. Frequently, the emission output is put in “arbitrary units”, due to the difficulty in calibrating the detection system accurately.

In both luminescence measurements and absorption measurements, a beam-splitting chopper can be realized. After detection in the phototube, phase sensitive detection and amplification is used to obtain a signal. Chopping at a pre-selected frequency allows narrowband amplification of the detected signal. Noise in the signal is limited to a narrow band centered at the chopping frequency.

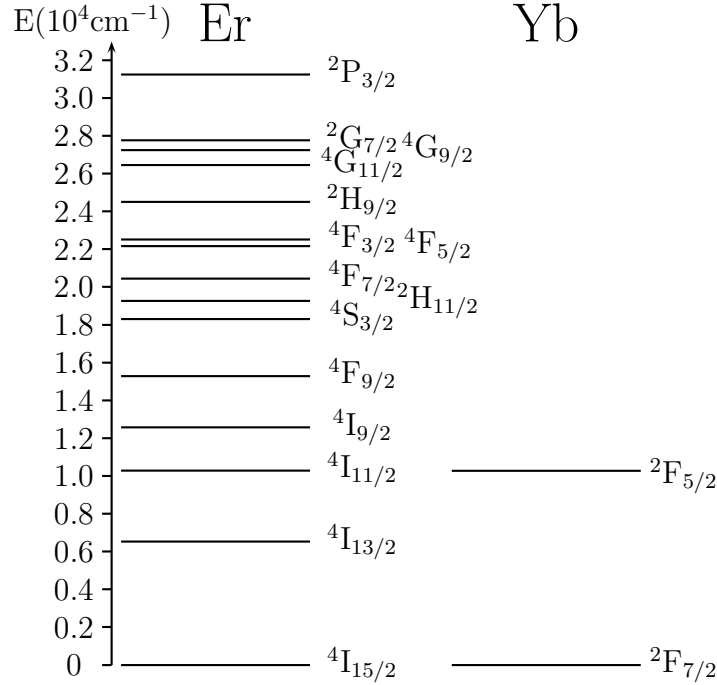


Figure 3.4: Classical Erbium Dieke diagram obtained from absorption peak spectrum

3.2.1 Emission Spectroscopy Procedure

The upconversion spectra was obtained with a conventional set up [46, 47] (sketched below in Fig. 3.5) Two NIR excitation pump sources were used: Ten nanoseconds pulsed tunable Optical Parametric Oscillator (MOPO from Spectra Physics) pumped by the third harmonic of Nd: YAG pulsed laser and a 967 nm laser diode LDD-9A (from ATC semiconductor devices). The fluorescence emission was analyzed with an Acton Pro 500i monochromator and an R955 Hamamatsu photomultiplier tube connected to mode-locking amplifier SR830 (Stanford Research Systems). The system was controlled with a PC where the emission spectra was displayed and recorded. All photoluminescence measurements were done at room temperature, and the samples were put in 1 mm diameter capillary tube to guarantee the same volume of excited material. The alignment of the set up was carefully maintained in order to compare the intensity of the up-converted signal between different characterized samples.

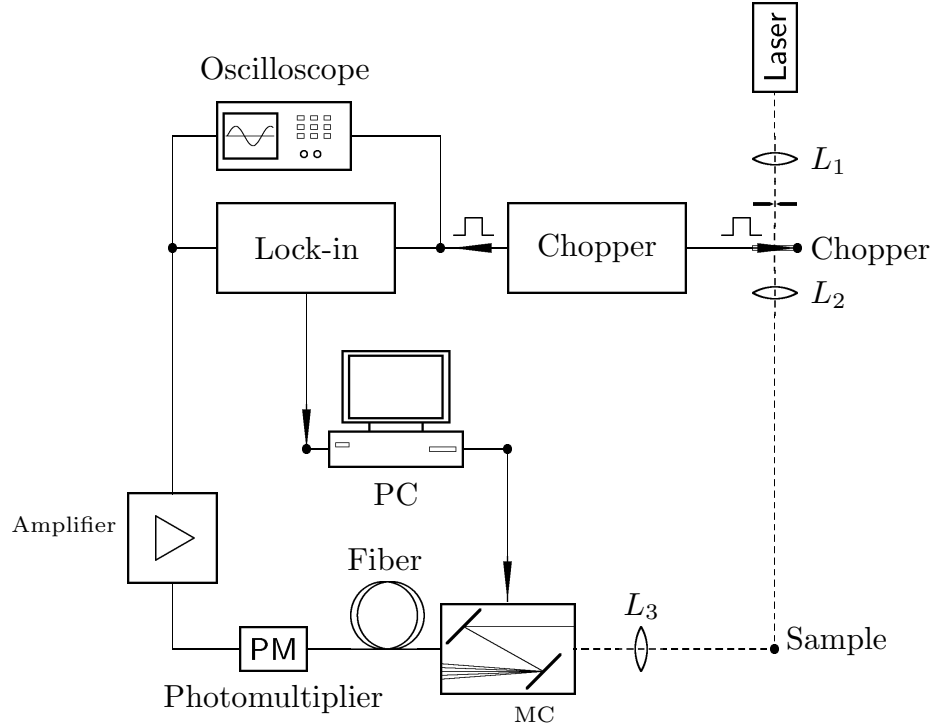


Figure 3.5: Experimental set up for up conversion emission spectroscopy

3.2.2 Emission Spectroscopy Results and Discussions

Under NIR excitation between 900 and 1050nm, upconversion emission in the UV (${}^4G_{11/2} \rightarrow {}^4I_{15/2}$), blue (${}^2P_{3/2} \rightarrow {}^4I_{13/2}$), green (${}^4S_{3/2} + {}^2H_{11/2} \rightarrow {}^4I_{15/2}$), and red (${}^4F_{9/2} \rightarrow {}^4I_{15/2}$) regions was observed for the codoped Er – Yb BaZrO₃ sample. Figure 3.6 below depicts these emission bands for various excitations wavelengths. The observed excitation trend suggests that there are at least three local excitation maxima at 979, 939, and 920nm for BZO:Er(1%),Yb(2%). These excitation peaks match the absorption peaks of the broad absorption band of BaZrO₃ : Er – Yb around 960nm. Whereas two wavelength excitation minima are in 933 and 944 nm.

If these three emission bands (UV-blue, green, and red) are integrated, the histogram in Fig. 3.7 can be made. This is done in order to compare the different emission bands dependence on excitation wavelength. The observed values for maxima and minima are for all emission bands.

Although the three emission bands seem to follow the same tendency, there are slight differences. Figure 3.8 shows the blue to green and red to green ra-

CHAPTER 3. OPTICAL SPECTROSCOPY

3.2. EMISSION SPECTROSCOPY

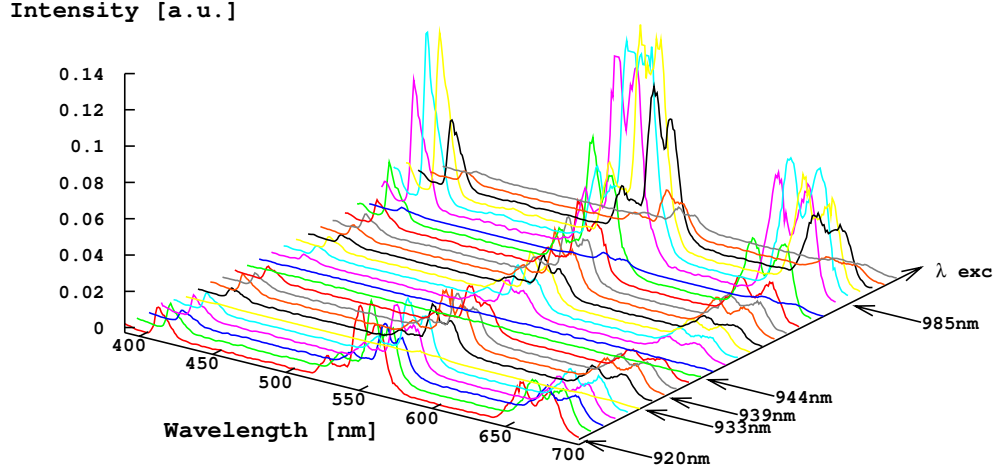


Figure 3.6: Visible emission when the wavelength of the pumping is varied.

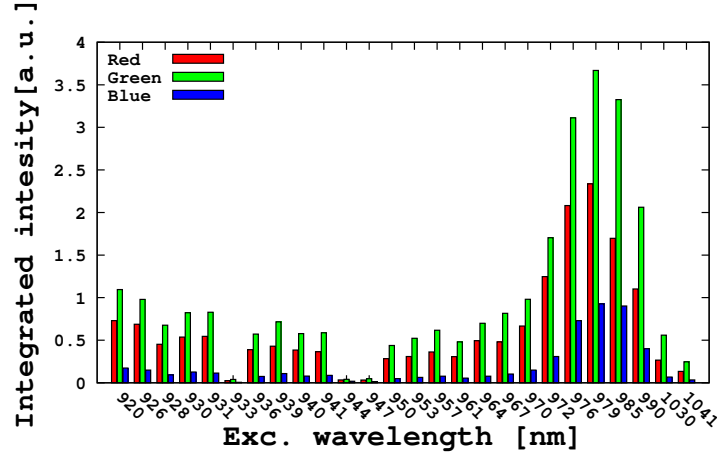


Figure 3.7: Integrated intensity vs excitation wavelength varied.

tios ($I(\text{blue})_{\text{integral}}/I(\text{green})_{\text{integral}}$, $I(\text{red})_{\text{integral}}/I(\text{green})_{\text{integral}}$), respectively, for all the observed excitation wavelength range. The blue to green emission ratio has a local maxima in 985 nm whereas the red to green emission ratio has it at 970 nm. Nevertheless, both ratios have the main maxima at 944 nm, corresponding

CHAPTER 3. OPTICAL SPECTROSCOPY

3.2. EMISSION SPECTROSCOPY

to one of the principal absorption peaks of Yb^{3+} . That suggest that in fact Yb^{3+} acts as a very good sensitizer of Er^{3+} in BZO. As a consequence of this behavior, a tunable rate emission is possible when excitation wavelength is changed.

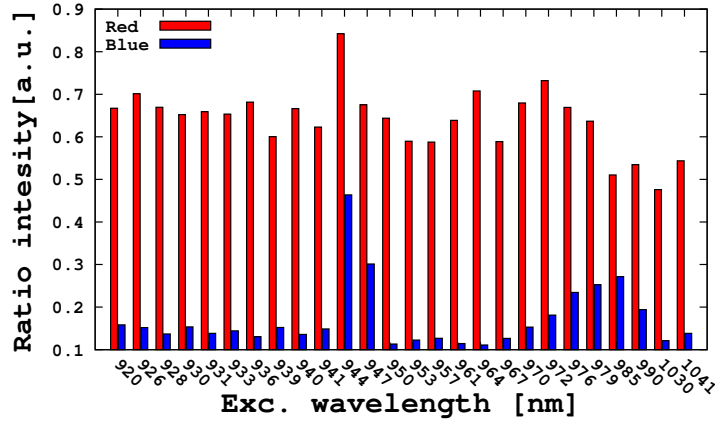


Figure 3.8: Integrated intensity of normalized ratio emission blue/green and red/green.

Figure 3.9 shows the upconversion emission spectra for increasing NIR pump power at 967nm for the case of Yb – Er codoped BaZrO_3 . It is clear that UV-blue to red band emission increases as the pump power increases.

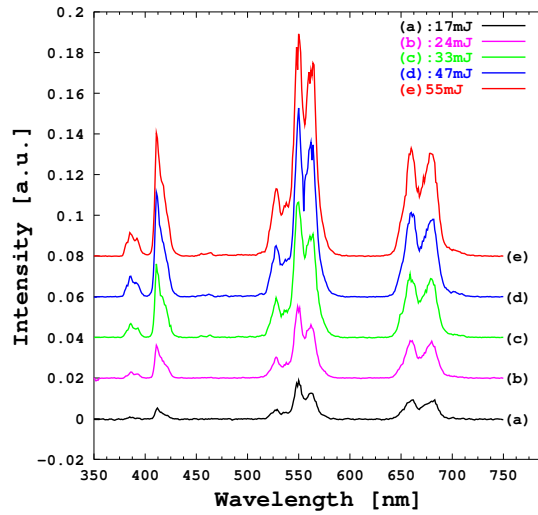


Figure 3.9: Visible up converted emission when a power of pumping is increased.

CHAPTER 3. OPTICAL SPECTROSCOPY

3.2. EMISSION SPECTROSCOPY

The dependence of the up-converted integrated signal intensity (I_{upc}) for each observed emission band is analyzed as a function of the pumping intensity (I_{pump}), see Fig. 3.10. It is well known that this dependence can be expressed as [48, 49]:

$$I_{upc} = k I_{pump}^n,$$

where n denotes the number of photons absorbed to produce such up-converted emission band. It is interesting to note that for all three bands $n \cong 2$. This suggests that all the three observed up-converted emission require the successive excitation of Er ions by absorbing two NIR excitation photons (976nm). That can be directly understood for the green and red emissions [50, 51] ; however for the UV- blue band, it should take up to four pump photons to populate the $^2P_{3/2}$ level. Such event seems to be less probable to happen by cascading the up-conversion process. On the other hand, if we assume that the cooperative processes of Yb ions as well as the cross relaxation of Er ions are quite strong and fast, then above proposed energy transfer process from the excited Yb dimmers into the $^4I_{13/2}$ level of Er will take place. The observed dependence on power suggest that this energy transfer process should follow the dynamics of population of the red band, since it depends completely on the success of the cross relaxation process.

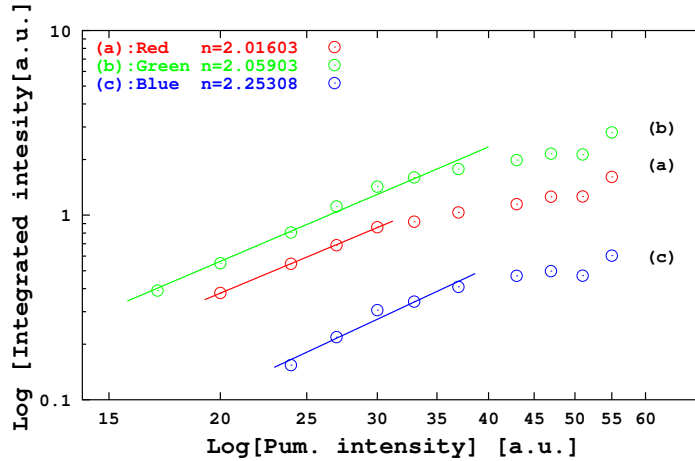


Figure 3.10: Integrated intensity bands when a power of pumping is varied.

It is important to point out that an Er single doped BaZrO₃ sample for an excitation power of 17mJ, the typical green emission is almost negligible and that the main up-converted emission corresponds to the red band. Therefore this could be explained as the fact that a 1%mol Er doping corresponds to the concentration

CHAPTER 3. OPTICAL SPECTROSCOPY

3.2. EMISSION SPECTROSCOPY

limit for which the cross relaxation process:

$$(^2H_{11/2}, ^4I_{15/2}) \rightarrow (^4I_{9/2}, ^4I_{13/2}), \quad (3.4)$$

is maximum, and results in the saturation of the $^4I_{13/2}$ (Er) level. Then a second up-conversion process

$$(^4I_{13/2}, ^4I_{11/2}) \rightarrow (^4F_{9/2}, ^4I_{15/2}), \quad (3.5)$$

results in the increased emission of the red band ($^4F_{9/2} \rightarrow ^4I_{15/2}$, see Fig. 3.12).

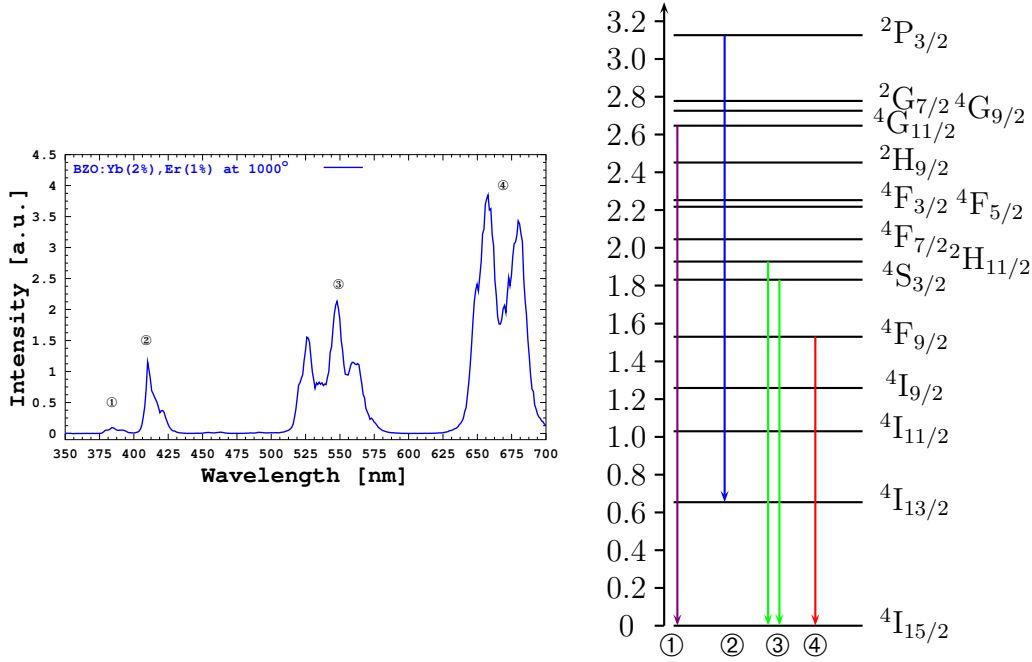


Figure 3.11: Up conversion emission spectra of BaZrO₃ : Yb(2%)Er(1%) irradiated at 967 nm (left) and involves emission transitions of Er ion (right).

When the codoped Yb – Er BZO is irradiated at continuous wave of IR diode at 967 nm, the upconversion emission is obtained in the UV ($^4G_{11/2} \rightarrow ^4I_{15/2}$), blue ($^2P_{3/2} \rightarrow ^4I_{13/2}$), green ($^4S_{3/2} + ^2H_{11/2} \rightarrow ^4I_{15/2}$), and red ($^4F_{9/2} \rightarrow ^4I_{15/2}$) regions as is depicted in Fig. 3.11.

In the codoped Er – Yb BaZrO₃ sample, we assume that in addition to the presence of the cross relaxation among Er ions, cooperative excitation of Yb dimmers (Yb^{*}) takes place[†]. Once an Yb dimer is in its ground state ($2\ ^2F_{7/2}[\text{Yb}^*]$) is excited to its upper level ($2\ ^2F_{5/2}[\text{Yb}^*]$) by the simultaneous absorption of two

[†]An Yb dimer is a couple of two Yb atoms that are so close that forms a molecular system [52].

CHAPTER 3. OPTICAL SPECTROSCOPY

3.2. EMISSION SPECTROSCOPY

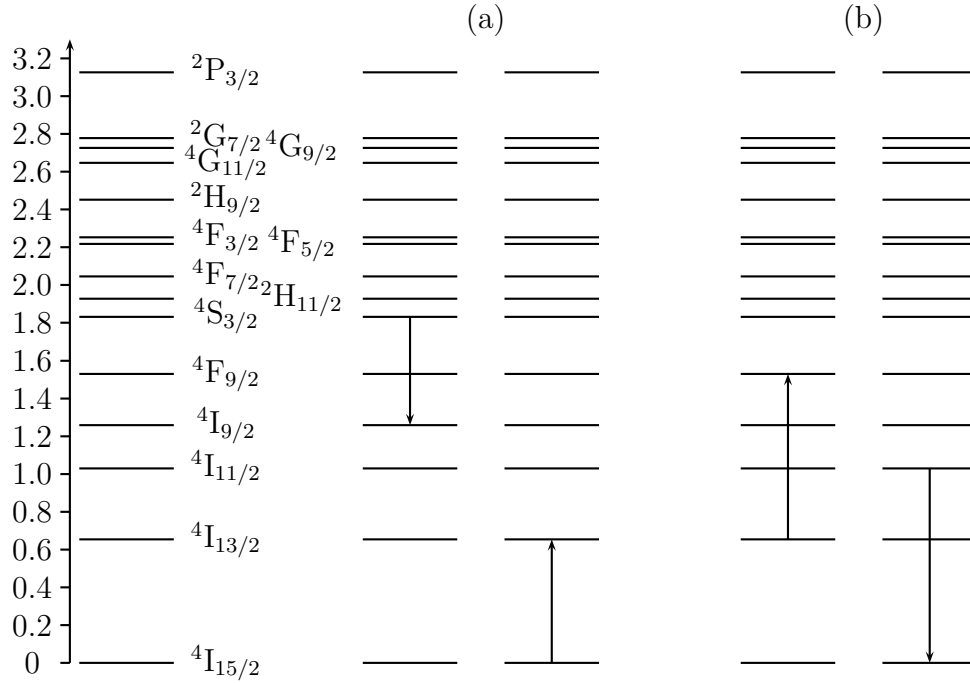
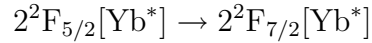
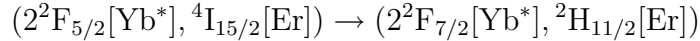


Figure 3.12: Cross relaxation process in (a) and Up conversion process in (b). Both process are improved in 1% Er, 2% Yb

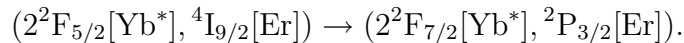
pumping photons, it can either emit one photon in the green band



or transfer its excitation to a neighboring Er ion. On the other side, if a neighboring Er ion is at its ground state then an energy transfer process



can take place, leading to the well known green emission band from the Er mixed level $2H_{11/2} + 4S_{3/2}$. Likewise, if the $4I_{9/2}[Er]$ level is already saturated by cross relaxation, then one electron at this level can promote to the $2P_{3/2}$ excited state by the energy transfer process



Two ions system needs to be considered as a single molecule in the sense of quantum mechanics because the overlap of the wavefunctions of the active electrons. Ishii has proposed that Yb dimmer formation is enhanced by the presence of oxygen and the cooperative emission is due to real eigenstate of the quantum dimmer system [53, 54, 55].

CHAPTER 3. OPTICAL SPECTROSCOPY

3.2. EMISSION SPECTROSCOPY

Then a partial radiative relaxation of this level leads to the observed blue emission ($^2P_{3/2} \rightarrow ^4I_{13/2}$) and a partial non radiative relaxation populates the next lower level $^4G_{11/2}$ that in turn radiatively relaxes producing the observable UV emission band ($^4G_{11/2} \rightarrow ^4I_{15/2}$). The maximum phonon energy of $BaZrO_3$ is around 587 cm^{-1} ($17.036\mu\text{m}$ or 0.072971eV), and the energy gap between the $^2P_{3/2}$ and the $^4G_{11/2}$ ion levels is around 4100cm^{-1} . Therefore, the non radiative relaxation from the $^2P_{3/2}$ to the $^4G_{11/2}$ level should be quite small since there is a need of more than seven lattice phonons to bridge the energy gap. As was discussed in Chapter one, this gap can be adjusted significantly with temperature. However, the UV emission observed is rather considerable and in consequence there must be additional channels of non radiative relaxation. Those channels can be provided by the large modes of residual OH- impurities on the surface of the nanocrystals. The existence of OH⁻ is related with the quenching mechanism [56]. Chemically, fluorides and OH⁻¹ are excluded. However, in oxides OH⁻¹ have been shown to exist. Because of this, the typical higher decay time in fluorides, with respect to garnets and oxides in general seem to be associated with the absence of OH⁻¹ impurities proved in the fluoride hosts.

The blue emission ($^2P_{3/2} \rightarrow ^4I_{13/2}$) of $BaZrO_3:Er$ has potential advantages for practical laser applications [57]. The transition terminates at the intermediate level $^4I_{13/2}$ of the Er ion, providing a four-level system for laser operation. It is well known that the $4f-4f$ transitions arising from forced electric dipole are parity forbidden and become partially allowed when the ion is situated at the low symmetry site. Thus, a lowering in the site symmetry of the ion will produce enhancement in optical transition probabilities. For nanocrystalline $BaZrO_3$ the high specific surface area results in a large number of atoms near of the surface with obviously smaller next nearest neighbor coordination. This leads to strong cross relaxation and cooperative process (dimmer formation) among rare earth ions. Furthermore, the crystal lattice near the particle surface tends to transform into structures of lower symmetry that increases the optical transition. As a nanocrystallite size decreases, more rare earth ions are distributed onto or near the surface due to the diffusion effect. For Er ions it means that transitions probabilities of ($^2P_{3/2} \rightarrow ^4I_{13/2}$) may be enhanced by controlling the growth of nanoparticles during synthesis. Since there is a wide energy gap between the $^2P_{3/2}$ and $^2G_{7/2}$ level, multi-phonon relaxation from the $^2P_{3/2}$ level to the lower one will be very small if the hydroxyl residual groups located on the nanocrystalline surface are effectively eliminated. Therefore, a higher quantum efficiency of the blue band emission is possible.

$BaZrO_3:Yb^{3+}$ samples emit in the green band and its emission could be observed at naked eye. It is important to point out that normal NIR Yb^{3+} luminescence is expected around 1030 nm , but if was present, it was not possible to detect it with our set up. Assuming Yb^{3+} ions are excited at its $^4F_{9/2}$ upper level, green emission can result from cooperative Yb ion pairs can lead to the green emission, centered around 505 nm , shown in Figure 3.13. The peak at 483nm does not correspond

CHAPTER 3. OPTICAL SPECTROSCOPY

3.2. EMISSION SPECTROSCOPY

to a harmonic of the pump excitation at 967nm. To verify this, a band pass filter (400nm-700nm) was set before the monochromator so spurious excitation light did not interfere with the measurements.

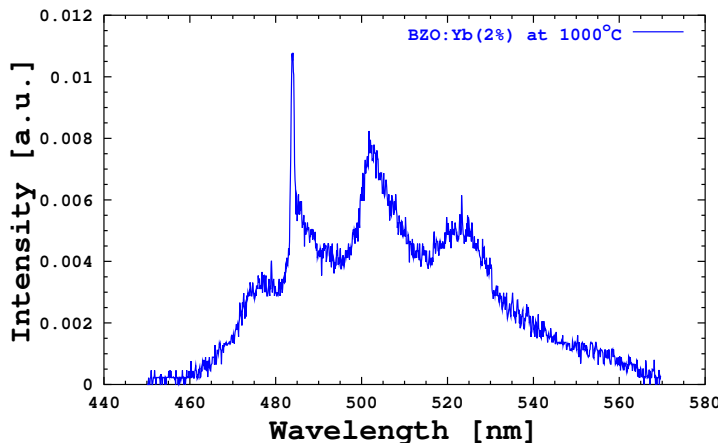


Figure 3.13: Cooperative emission of Yb pairs in BaZrO_3 .

It is interesting to note the lack of detectable NIR emission from BZO:Yb, whereas under the same conditions we were able to observe the NIR Yb emission. For the emission spectra of BZO:Yb, it was not observed since non significant emission could be detected as in other Yb doped samples like zirconia (ZrO_2) and YAG host, see Fig. 3.14. This absence of IR emission has been interpreted as a quasi-total energy transfer to cooperative processes since all radiative emissions arise in visible region.

Final Comments

The visible luminescent upconversion properties of erbium ytterbium doped barium zirconate were inquired. It was possible to obtain three visible bands: UV-blue, green, and red emission were present under IR pumping. The possible upper levels population mechanism were explained using Er – Yb Dieke diagram. The role of Yb is to act as a sensitizer in an efficient way in order to transfer its accumulated energy into the Er ion which provides the upper levels to obtain upconversion in the visible range. This feature of BZO leads to consider it as a good candidate to nanophosphor labeling. In biological applications is necessary to get isolated bands, which can be achieved in further researches, the functionality of nanosized BZO as a host material for rare earths was shown in this work.

CHAPTER 3. OPTICAL SPECTROSCOPY

3.2. EMISSION SPECTROSCOPY

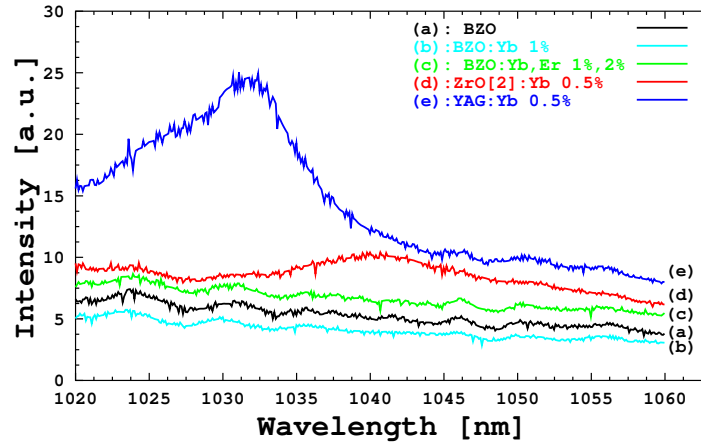


Figure 3.14: Typical infrared emission spectra of BZO is not detectable unlike other samples such as (d) $\text{ZrO}_2\text{:Yb}$ and (e) YAG:Yb .

Chapter 4

Conclusions

In this thesis work, well defined nanocrystallites rare-earth doped and undoped barium zirconate were obtained at low temperature by an hydrothermal process as well as at low cost. We found that the synthesis process is reliable since the structure, cubic crystalline phase, and morphology are consistent in spite of high rare earth concentration doping and the annealing treatment up to 1000°C. Also, there is not additional segregation, or appreciable lattice distortion. Furthermore, it was shown that the annealing increases the crystallinity of nanocrystallites of barium zirconate, but it also increases the particle size. Within this scope, for high power laser is desirable that the structural properties of the host remain constant under a wide range of power flux in order to have low loss mechanisms. Thus barium zirconate is a promising candidate to high power solid state laser devices. Adequate analysis in order to get the particle size, structure and crystalline phase were carried on and confirmed according to the x-ray diffraction, transmission electron microscopy, high resolution transmission electron microscopy and Fast Fourier Transform of the high resolution transmission electron microscopy.

Absorption spectroscopy studies on undoped barium zirconate showed that it is transparent in the visible range and it has a strong absorption in the near ultraviolet range and in the infrared region, this last peak is due to OH radicals and it showed attenuation when the annealing temperature was increase. Typical narrow absorption bands due to erbium and ytterbium are present in the corresponding doped samples. Also, the ultraviolet peak changes as annealing temperature increases. Here, it is split into two local maximum when the annealing temperature is 100°C but it is broaden into one single peak at 1000°C.

Strong ultraviolet, blue, green, and red visible upconversion emissions were achieved for nanocrystallites of ytterbium-erbium codoped barium zirconate when they were radiated with nano-pulsed infrared excitation. For single ytterbium doped barium zirconate it was observed the typical green cooperative emission -as it is expected- and the noticeable strong quenching of the infrared emission of both sin-

CHAPTER 4. CONCLUSIONS

gle doped ytterbium and for erbium-ytterbium codoped sample. Here, we proposed that efficient cooperative energy transference between a pair of ytterbium ions take place in both samples. While in the single erbium doped barium zirconate, the ultraviolet-blue emission was negligible. So, the addition of ytterbium as improves the mechanism in which the blue emission is attained, i.e. ytterbium can to act as a sensitizer of erbium. In this sense, when visible emission power dependence is inquired, for all three bands, we found that two incident photons are necessary to get the visible bands. This behavior is expected from red and green bands as it was explained in the chapter 3, but under the scheme exposed in same chapter for blue emission, this does not follow immediately. Here, we proposed that one cooperative green photon is added with one incident infrared photon. Also, the visible luminescence was investigated when the excitation pump wavelength was varied. Here, it was found that local maximum wavelength matched with the absorption spectra obtained. If a continuous wave infrared diode laser is used to promote visible up-conversion emission, there is a significative relative increase of the red band -respect to the other ones- in ytterbium-erbium codoped barium zirconate with respect to that obtained with the pulsed optical parametric oscillator source. This is due to the high electromagnetic density achieved by the MOPO improves the mechanism that populates the ultraviolet-blue levels.

Visible bands obtained can be used for biological labeling as long as one single emission is tunable. Special interest is in short wavelengths as ultraviolet-blue emission is observed in barium zirconate: ytterbium-erbium, so the principal goal is to isolate this mechanism by modifying the dynamics of the other levels (quench those emissions). This is the first time, to our knowledge, that both cooperative emission -due to ytterbium ions pairs- and up converted emissions from UV to red -from erbium, due to interactions between ytterbium-erbium ions- was obtained from barium zirconate host.

Some results obtained in this work have been presented in two meetings: 1) Third international topical meeting on Nanostructured materials and nanotechnology, in Puebla, Pue. México from September 24th to 28th, 2006. Oral presentation: "A new blue to red emitting nanophosphor: $\text{BaZrO}_3: \text{Er}, \text{Yb}$ ". 2) XLIX Congreso Nacional de Física San Luís Potosí 16th to 20th October, 2006, Oral presentation: "Nanocrystalline BaZrO_3 a new host for efficient Yb cooperative upconversion processes. 3) The work has been accepted as an oral presentation: "UV to Red cooperative enhanced upconversion in nanocrystalline $\text{BaZrO}_3: \text{Yb}^{3+}\text{Er}^{3+}$ ", for SPIE congress in San Diego.

Also part of those results were accepted to be published in Journal of Nanoscience and Nanotechnology: "A new blue, green, and red upconversion emitting nanophosphor: $\text{BaZrO}_3: \text{Er}, \text{Yb}$; L.A. Diaz-Torres, P.Salas, J.S. Perez-Huerta, C. Angeles-Chavez, E. De la Rosa-Cruz".

Appendix A

Barium Zirconate Face Ending

Because well faceted barium zirconate nanocrystallites morphology was observed in the hydrothermal method presented, a brief discussion on the possibilities of surface ending in a barium zirconate host can take place.

Barium zirconate nanoparticles can appear as a truncated octahedron [34]. It is important to distinguish between the typical decahedron morphology observed in ZrO_2 particles [58]. This octahedron shape has also been observed in nanoparticles of CeO_2 [59, 60]. In that case, theoretical modeling suggests that the $[1\ 1\ 1]$ plane is the most energetically favorable for ending in the CeO_2 structure followed by $[1\ 1\ 0]$, $[2\ 1\ 1]$ [61]. However, the $[1\ 1\ 1]$ plane is energetically unstable due to a net dipole moment normal to the surface.

The importance of the analysis of the $[1\ 1\ 1]$ and $[1\ 0\ 0]$ surfaces in the BZO and their stability lies in the recently interest of barium zirconate applications in electronics, fuel cells, and substrate materials. The surface termination in the barium zirconate as perfectly cleaved is shown in the figures through A.1- A.4. They were obtained from *Jmol* software with the help of *Mathlab* program.

The $[1\ 0\ 0]$ surface consists on layers that are electrically neutral (BaO or ZrO_2) and have not net dipole moment, see Fig. A.1. Some works suggest that these terminations are common in perovskites [45]. This termination surface has the lowest energy, requiring no further modification to the charges at its surface or in stoichiometry to preserve a nonpolar surface.

However, the $[1\ 1\ 0]$ surface consist on charged planes (sequence of $\text{O}_2 - \text{BaZrO} - \text{O}_2 - \text{BaZrO} -$, $-2, +4, -2, +4\dots$, respectively), see Fig. A.2 arranged symmetrically. When the termination is O_2 in the $[1\ 1\ 0]$ surface, it is supposed that it has infinite dipole moment perpendicular to the surface and thus unstable. If 50% oxygen was removed from the surface, the structure will remain with charged planes but zero net dipole moment.

The $[1\ 1\ 1]$ surface consists on alternating polar layers and of BaO_3^{4+} and Zr^{4+} , see Fig. A.3. This perovskite configuration has been almost not discussed in the

APPENDIX A. BARIUM ZIRCONATE FACE ENDING

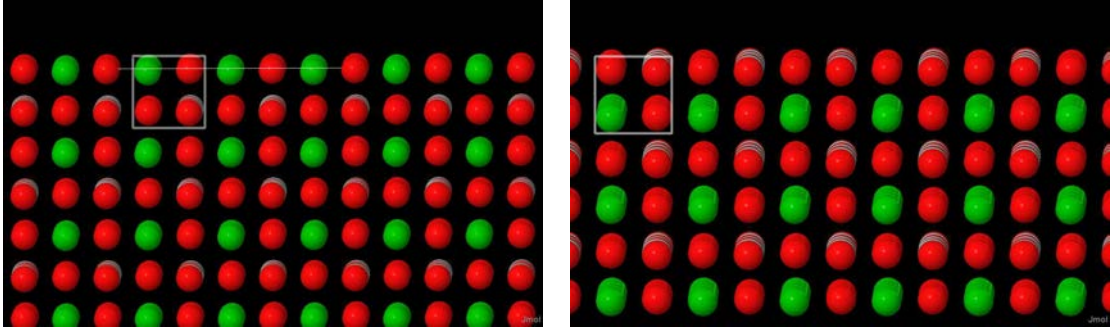


Figure A.1: Normal and tangential sight of the $[100]$ surface in BZO perovskite structure. Termination of this plane may either be on the BaO (left) or ZrO_2 (right). Red balls are O, green balls are Ba, and Zr are blue balls. The surface termination is the upper horizontal atoms arrange.

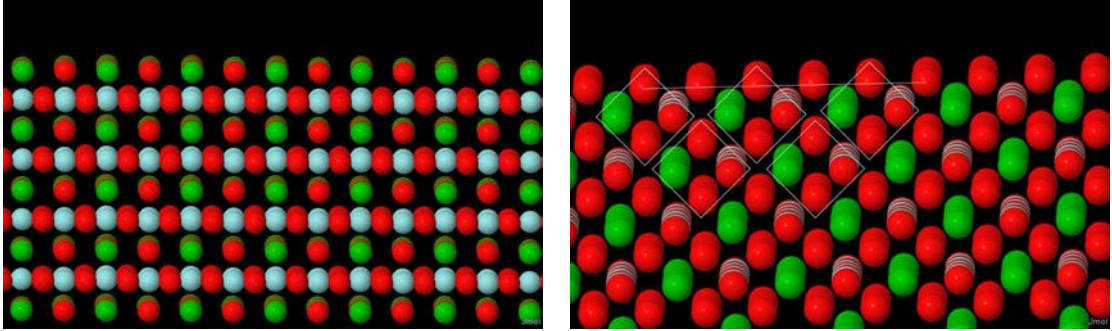


Figure A.2: Normal (left) and tangential (right) sight of the $[110]$ surface in BZO perovskite structure. Termination of this plane may either be on the O_2 (left) or BaZrO (left, sub-layer). Red balls are O, green balls are Ba, and Zr are blue balls.

literature being SrTiO_3 the most studied. This configuration has been possible by Ar bombardment and annealing at 1470 K in oxygen [62]. Scanning tunneling microscopy on BaTiO_3 had shown that the $[111]$ surface is producible. However BaO_3^{4+} or Zr^{4+} terminations could not be made. In the $[111]$ planes, the surface energy is relatively independent on surface composition and is higher than that for the $[110]$ planes [34]

Figure A.4 depicts the top view of $[011]$, as it was shown in the experimental TEM section. Is important to point out that works on the stability of that surface have not been developed yet. But experimental evidence has been provided in this thesis work.

Although in this section only qualitative and bibliography description was given. As a final conclusion, the lowest energy surface $[100]$ is the most probable to occur

APPENDIX A. BARIUM ZIRCONATE FACE ENDING

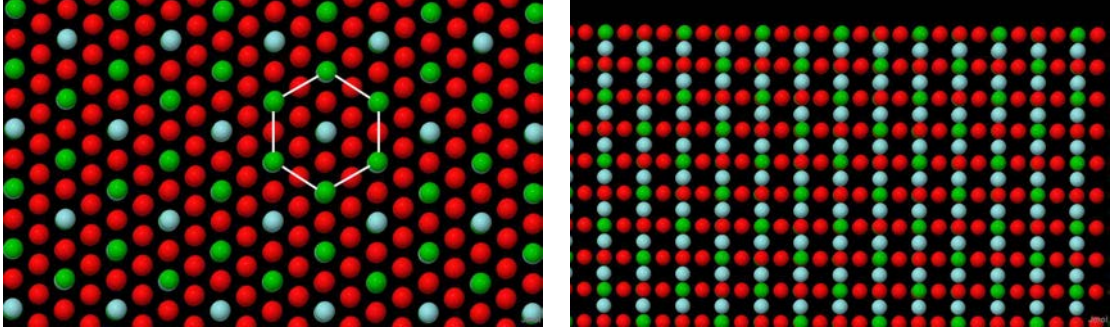


Figure A.3: Normal (left) and tangential (right) sight of the $[1\ 1\ 1]$ surface in BZO perovskite structure. Termination of this plane may either be on the BaO_3^{4+} or Zr^{4+} . Red balls are O, green balls are Ba, and Zr are blue balls.

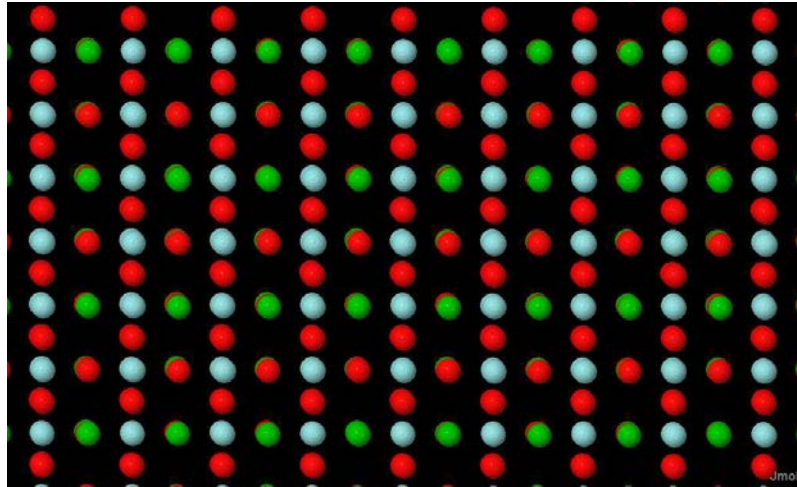


Figure A.4: Normal sight of the $[0\ 1\ 1]$ surface in BZO perovskite structure. Red balls are O, green balls are Ba, and Zr are blue balls.

because this minimal energy provides also the most stable structure. Also, other surface planes need to be calculated. However, further studies are needed to confirm this.

Appendix B

Additional XRD Results and Discussion

As it was already presented in Chapter 2, here we show x-ray diffraction patterns for BZO nanocrystalline annealing at 500 °C and as synthesized (100 °C) samples, Fig. B.1 and Fig. B.2, respectively.

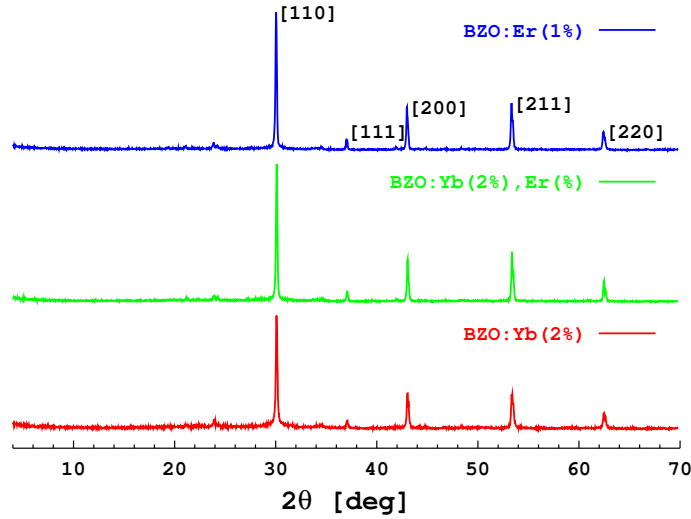


Figure B.1: XRD patterns of BaZrO_3 annealing at 500 °C. The bottom pattern corresponds to an Yb doped sample, the middle pattern corresponds to an Yb – Er codoped sample whereas the upper one corresponds to an Er doped sample

It is observed that the samples, synthesized at (100 °C), have high crystallinity and no additional phase was detected in either annealing at (500 °C) or (100 °C). As it was referred, barium zirconate has the phase stability with respect to the

APPENDIX B. ADDITIONAL XRD RESULTS AND DISCUSSION

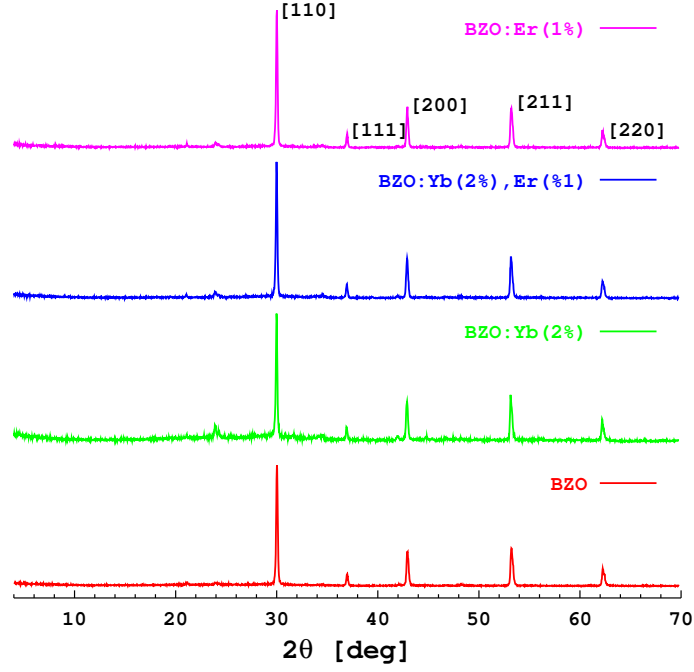


Figure B.2: XRD patterns of BaZrO₃ as synthesized. The upper patterns correspond to doped and codoped samples whereas the pattern at the bottom corresponds to undoped samples.

annealing temperature expected. Additional, phase is invariant with the doping concentration.

Appendix C

Energy Dispersive X-ray Spectroscopy (EDXS)

As it was pointed out in Chapter 2, also energy dispersive X-ray spectroscopy (EDXS) was performed. The physical principle of EDXS can be adapted also from the discussion in Chap. 2, but instead of dispersive electrons, x-ray radiation impinges upon the sample. In Fig. C, it is shown the EDXS spectra of Yb doped BZO, and two foreign elements are present: Na coming from precipitant sodium hydroxide, and Cl coming from precursor zirconyl chloride octahydrate.

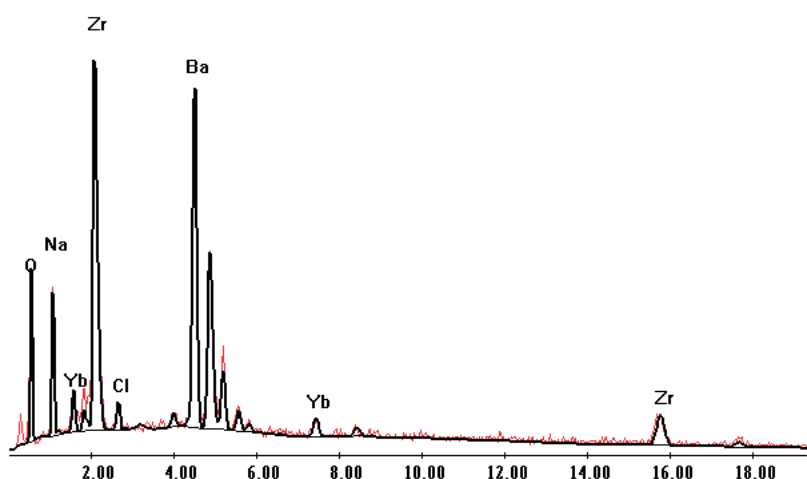


Figure C.1: EDXS spectra of BZO:Yb(2%) annealing at 500 °C. Abscise is in KeV.

While in Fig. C, barium zirconate annealing at 1000 °C lacks Cl and Na ele-

APPENDIX C. ENERGY DISPERSIVE X-RAY SPECTROSCOPY (EDXS)

ments, and other elements. So, this treat has purified the barium zirconate nanoparticles from residual compounds of the synthesis method.

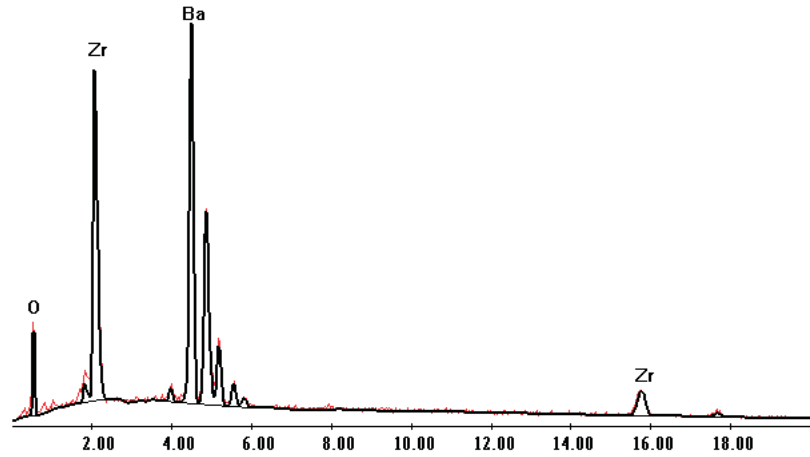


Figure C.2: EDXS spectra of Barium Zirconate powder annealing at 1000 °C. Abscise is in KeV.

Bibliography

- [1] G. Ali Mansoori. *Principles Of Nanotechnology: Molecular-based Study Of Condensed Matter In Small Systems*. World Scientific Pub, 2005.
- [2] De la Rosa, E., Salas, P., Díaz-Torres, L.A.; Martnez, and C. A.; Angeles. Strong visible cooperative up-conversion emission in $\text{ZrO}_2 : \text{Yb}^{3+}$ nanocrystals. *J. Nanosci/Nanotech*, 5(9):1480–1486, 2005.
- [3] L A Díaz-Torres, E De la Rosa-Cruz, P Salas, and C Angeles-Chavez. Concentration enhanced red upconversion in nanocrystalline $\text{ZrO}_2 : \text{Er}$ under ir excitation. *J. Phys. D: Appl. Phys.*, 37:2489–2495, 2004.
- [4] L.A. Diaz-Torres, E. De la Rosa, P. Salas, and H. Desirena. Enhanced cooperative absorption and upconversion in Yb^{3+} doped YAG nanophosphors. *optical materials*, 27(7):1305–1310, 2005.
- [5] Kenyon A.J. Recent developments in rare-earth doped materials for optoelectronics. *Progress in Quantum Electronics*, 26(4):225–284, 2002.
- [6] Michel J. F. Digonnet. *Rare-Earth-Doped Fiber Laser and Amplifiers*. Marcel Dekker, Inc.
- [7] Reid MF Duan CK. A simple model for $f \rightarrow d$ transitions of rare-earth ions in crystals. *Journal of Solid State Chemistry*, 171(1), 2003.
- [8] Kazuyoshi Ogasawara, Shinta Watanabe, Yuki Sakai, Hiroaki Toyoshima, Takugo Ishii, Mikhail G. Brik, and Isao Tanaka. Calculations of complete $4f^n$ and $4f^{n-1} 5d^1$ energy level schemes of free trivalent rare-earth ions. *Japanese Journal of Applied Physics*, 43(5A):L611–L613, 2004.
- [9] Víctor Eduardo López Padilla. *Modelado y Caracterización de Fibras Ópticas Dopadas con Erblio para sensores basados en Fluorescencia*. PhD thesis, Centro De Investigaciones En Óptica A.C., 2006.
- [10] G. Y. Chen, Y. G. Zhang, G. Somesfalean, Z. G. Zhang, Q. Sun, and F. P. Wang. Two-color upconversion in rare-earth-ion-doped ZrO_2 nanocrystals. *Applied Physics Letters*, 89(16):163105, 2006.

- [11] David O. Solis Santana. Luminescence properties of $\text{ZrO}_2 : \text{Yb}^{3+}\text{Er}^{3+}$ nanocrystals. Master's thesis, Centro De Investigaciones En Óptica A.C., 2006.
- [12] Luis Octavio Meza Espinoza. Pair driven ir fluorescence quenching of Yb^{3+} in $\text{ZrO}_2 : \text{Yb}^{3+}$. Master's thesis, Centro De Investigaciones En Óptica A.C., 2006.
- [13] Pushpal Ghosh and Amitava Patra. Understanding the influence of nanoenvironment on luminescence of rare-earth ions. *Pramana, J. of physics*, 65(5):901, 2005.
- [14] Azuel François. Upconversion and anti-stokes processes with f and d ions in solids. *Chemical Reviews*, 104(1):139–174, 2004.
- [15] J. Amami, D. Hreniak, Y. Guyot, R. Pazik, C. Goutaudier, G. Boulon, M. Ayadi, and W. Strek. Second harmonic generation and Yb^{3+} cooperative emission used as structural probes in size-driven cubic-tetragonal phase transition in BaTiO_3 sol-gel nanocrystals. *Journal of Luminescence*, 119-120:383–387, 2006.
- [16] X. L. Ruan and M. Kaviany. Enhanced laser cooling of rare-earth-ion-doped nanocrystalline powders. *Phys. Rev. B*, 73:155422, 2006.
- [17] Per G. Sundell, Mrten E. Bjorketun, and Goran Wahnstrom. Thermodynamics of doping and vacancy formation in BaZrO_3 perovskite oxide from density functional calculations. *Physical Review B (Condensed Matter and Materials Physics)*, 73(10):104112, 2006.
- [18] Babilo Peter and Haile Sossina M. Enhanced sintering of yttrium-doped barium zirconate by addition of ZnO . *Journal of the American Ceramic Society*, 88(9):2362–2368, 2005.
- [19] Luis de la Peña. *Introducción a la Mecánica Cuántica*. FONDO DE CULTURA ECONOMICA, 3 edition, 2006.
- [20] Luis de la Peña. *Problemas y Ejercicios de Mecánica Cuántica*. FONDO DE CULTURA ECONOMICA, 3 edition, 2006.
- [21] B. Henderson and G. F. Imbusch. *Optical Spectroscopy of Inorganic Solids*. Oxford University Press, 1981.
- [22] Guokui Liu and Bernard Jacquier. *Spectroscopic Properties of Rare Earths in Optical Materials*. Springer Series in Materials Science, 2005.
- [23] F. Varsanyi and G. H. Dieke. Ion-pair resonance mechanism of energy transfer in rare earth crystal fluorescence. *Phys. Rev. Lett.*, 7(12):442, 1961.

- [24] Eiichiro Nakazawa and Shigeo Shionoya. Cooperative luminescence in YbPO_4 . *Phys. Rev. Lett.*, 25(25):1710–1712, 1970.
- [25] P. P. Feofilov and V. V. Ovsyankin. Cooperative luminescence of solids. *Appl. Opt.*, 6(11):1828, 1967.
- [26] Stefan R. Lüthi, Markus Pollnau, Hans U. Güdel, and Markus P. Hehlen. Near-infrared to visible upconversion in Er^{3+} -doped $\text{Cs}_3\text{Lu}_2\text{Cl}_9$, $\text{Cs}_3\text{Lu}_2\text{Br}_9$, and $\text{Cs}_3\text{Y}_2\text{I}_9$ excited at $1.54\text{ }\mu\text{m}$. *Phys. Rev. B*, 60(1):162–178, 1999.
- [27] Robert G. Parr and Weitao Yang. *Density-Functional Theory of Atoms Molecules*. Oxford University Press, 1989.
- [28] J. Michael Hollas. *Basic Atomic and Molecular Spectroscopy*. Wiley Interscience, 2002.
- [29] Robert D Cowan. *The Theory of atomic Structure and Spectra*. Berkeley: University California Press., 1981.
- [30] C. Cohen-Tannoudji, Frank Laloe, and Bernard Diu. *Quantum Mechanics*, volume I. Wiley-Interscience, 1977.
- [31] C. Cohen-Tannoudji, Bernard Diu, and Frank Laloe. *Quantum Mechanics*, volume II. Wiley-Interscience, 1977.
- [32] Zhenwen Dai Renjun Xu. Alternative mathematical technique to determine ls spectral terms. *Journal Physics B*, 39:3221–3239, 2006.
- [33] F. Boschini, B. Robertz, A. Rulmont, and R. Cloots. Preparation of nanosized barium zirconate powder by thermal decomposition of urea in an aqueous solution containing barium and zirconium, and by calcination of the precipitate. *Journal of the European Ceramic Society*, 23(16):3035–3042, 2003.
- [34] Keith J. Leonard, Srivatsan Sathyamurthy, and M. Parans Paranthaman. Characterization of BaZrO_3 nanoparticles prepared by reverse micelle synthesis. *Chemistry of materials*, 17(15):4010–4017, 2005.
- [35] Z. Lu, Y. Tang, L. Chen, and Y. Li. Shape-controlled synthesis and characterization of BaZrO_3 microcrystals. *J. Cryst. Growth*, 266:539, 2004.
- [36] M. Veith, S. Mathur, N. Lecerf, V. Huch, T. Decker, H. P. Beck, W. Eiser, and Haberkorn. Sol-gel synthesis of nano-scaled BaTiO_3 , BaZrO_3 and $\text{BaTiO}_{0.5}\text{Zr}_{0.5}\text{O}_3$ oxides via single-source alkoxide precursors and semi-alkoxide routes. *J. Sol-Gel Sci. Technol*, 15:145, 2000.

- [37] B. Guillaume, F. Boschini, I. Garcia-Cano, A. Rulmont, R. Cloots, and M. Ausloos. Optimization of BaZrO₃ sintering by control of the initial powder size distribution; a factorial design statistical analysis. *Journal of the European Ceramic Society*, 25(16):3593–3604, 2005.
- [38] Richard T. Weidner and Robert L. Sells. *Elementary Modern Physics*. Allyn and Bacon, 3 edition, 1980.
- [39] Neil W. Ashcroft and N. David Mermin. *Solid State Physics*. Holt Rinehart and Winston, 1976.
- [40] Markus Winterer. *Nanocrystalline Ceramics: Synthesis and Structure*. Springer Verlag, 2002.
- [41] Ludwing Reimer. *Scanning Electron Microscopy*. Springer Series in Optical Sciences, 1985.
- [42] Maths Karlsson, Mårten E. Björketun, Per G. Sundell, Aleksandar Matic, Göran Wahnström, Dennis Engberg, Lars Brjesson, Istaq Ahmed, Sten Eriksson, and Pedro Berastegui. Vibrational properties of protons in hydrated BaIn_xZr_{1-x}O_{3-x/2}. *Physical Review B*, 72:094303–1–7, 2005.
- [43] E. Montoya, F. Agullo-Rueda, S. Manotas, J. Garcia Sole, and L. E. Bausa. Electron-phonon coupling in Yb³⁺ : LiNbO₃ laser crystal. *Journal of Luminescence*, 94-95:701–705, 2001.
- [44] Tomislav Biljan, Sanda Roncevic, Zlatko Meic, and Kristina Kovac. Non-vibrational features in nir ft-raman spectra of lanthanide sesquioxides. *Chemical Physics Letters*, 395(11):246–252, 2004.
- [45] J. Padilla and David Vanderbilt. Ab initio study of BaTiO₃ surfaces. *Physical Review B*, 56(3), 1997.
- [46] David W. Ball. *The Basics of Spectroscopy*. Spie Press, 2001.
- [47] David W. Ball. *Field Guide to Spectroscopy*. Spie Press, 2006.
- [48] M. Pollnau, D. R. Gamelin, S. R. Lüthi, H. U. Güdel, and M. P. Hehlen. Power dependence of upconversion luminescence in lanthanide and transition-metal-ion systems. *Phys. Rev. B*, 61(5):3337–3346, Feb 2000.
- [49] J. F. Suyver, A. Aebischer, S. Garcia-Revilla, P. Gerner, and H. U. Gudel. Anomalous power dependence of sensitized upconversion luminescence. *Physical Review B (Condensed Matter and Materials Physics)*, 71(12):125123, 2005.

- [50] Ralph A. Hewes and James F. Sarver. Infrared excitation processes for the visible luminescence of Er^{3+} , Ho^{3+} , and Tm^{3+} in Yb^{3+} -sensitized rare-earth trifluorides. *Phys. Rev.*, 182(2):427–436, 1969.
- [51] Siguo Xiao, Xiaoliang Yang, X.H. Yan, and Zhengwei Liu. Violet up-converted emission in $\text{Er}^{3+} : \text{Y}_2\text{O}_3$ nanocrystals. *Physics Letters A*, 343(1-3):90–94, 2005.
- [52] J. F. Suyver, R. Meester, J. J. Kelly, and A. Meijerink. A theory waiting for an experiment: pair-state formation in a nanocrystal. *Journal of Luminescence*, 102-103:182–188, 2003.
- [53] T. Ishii, M. G. Brik, and K. Ogasawara. First-principles analysis method for the multiplet structures of rare-earth ions in solids. *Journal of Alloys and Compounds*, 380(1-2):136–140, 2004.
- [54] Ishii Takugo. First-principles calculations for the cooperative transitions of Yb^{3+} dimer clusters in $\text{Y}_3\text{Al}_5\text{O}_{12}$ and Y_2O_3 crystals. *J Chem Phys*, 122(2):024705, 2005.
- [55] Harvey J. Schugar, Edward I. Solomon, William L. Cleveland, and Lionel Goodman. Simultaneous pair electronic transitions in Yb_2O_3 . *Journal of the American Chemical Society*, 97(22):6442–6450, 1975.
- [56] Y. Guyot, H. Canibano, C. Goutaudier, A. Novoselov, A. Yoshikawa, T. Fukuda, and G. Boulon. Yb^{3+} -doped $\text{Gd}_3\text{Ga}_5\text{O}_{12}$ garnet single crystals grown by the micro-pulling down technique for laser application. part 2: Concentration quenching analysis and laser optimization. *Optical Materials*, 28(1-2):1–8, 2006.
- [57] I. A. Grishin, V. A. Guryev, A. P. Savikin, and N. B. Zvonkov. Up-conversion luminescence in Er^{3+} and Yb^{3+} -doped fluorozirconate glasses. *Optical Fiber Technology*, 1(4), 1995.
- [58] Yacamán José and M Ascencio. *Handbook of Nanostructured Materials and Nanotechnology*, volume 2. Academic Press, 2000.
- [59] Lijun Wu, H. J. Wiesmann, A. R. Moodenbaugh, R. F. Klie, Yimei Zhu, D. O. Welch, and M. Suenaga. Oxidation state and lattice expansion of CeO_{2-x} nanoparticles as a function of particle size. *Physical Review B*, 69(12):125415, 2004.
- [60] Feng Zhang, Qiang Jin, and Siu-Wai Chan. Ceria nanoparticles: Size, size distribution, and shape. *Journal of Applied Physics*, 95(8):4319–4326, 2004.

- [61] D. C. Sayle, T. X. T. Sayle, S. C. Parker, C. R. A. Catlow, and J. H. Harding. Effect of defects on the stability of heteroepitaxial ceramic interfaces studied by computer simulation. *Phys. Rev. B*, 50(19):14498–14505, Nov 1994.
- [62] Wei Jen Lo and G. A. Somorjai. Temperature-dependent surface structure, composition, and electronic properties of the clean $\text{SrTiO}_3(111)$ crystal face: Low-energy-electron diffraction, auger-electron spectroscopy, electron energy loss, and ultraviolet-photoelectron spectroscopy studies. *Phys. Rev. B*, 17(12):4942–4950, 1978.
- [63] G. Boulon and V. Lupei. Energy transfer and cooperative processes in Yb^{3+} -doped cubic sesquioxide laser ceramics and crystals. *Journal of Luminescence*, 125:1–10, 2006.
- [64] Dammak M. and Zhang De-Long. Spectra and energy levels of Er^{3+} in Er_2O_3 powder. *Journal of alloys and compounds*, 407(1-2):8–15, 2006.
- [65] Daniela Di Martino, Anna Vedda, Giuliano Angella, Michele Catti, Elena Cazzini, Norberto Chiodini, Franca Morazzoni, Roberto Scotti, and Giorgio Spinolo. Evidences of rare earth ion aggregates in a sol-gel silica matrix: The case of cerium and gadolinium. *Chem. Mater*, 16(17):3352–3356, 2004.
- [66] Rakesh Kapoor, Christopher S. Friend, Abani Biswas, and Paras N. Prasad. Highly efficient infrared-to-visible energy upconversion in $\text{Er}^{3+} : \text{Y}_2\text{O}_3$. *Optics Letters*, 25(5):338–340, 2000.
- [67] V. M. Marchenko. Visible luminescence of Er_2O_3 induced by CO_2 laser radiation with a wavelength of $10.6 \mu\text{m}$. *Laser Physics*, 16(6):981–984, 2006.
- [68] K. Ogasawara, S. Watanabe, H. Toyoshima, T. Ishii, M.G. Brik, H. Ikeno, and I. Tanaka. Optical spectra of trivalent lanthanides in LiYF_4 crystal. *Journal of Solid State Chemistry*, 178(2):412–418, 2005.
- [69] Xun Wang, Jing Zhuang, Qing Peng, and Yadong Li. A general strategy for nanocrystal synthesis. *Nature*, 437:121–124, 2005.
- [70] M. Yu, J. Lin, Z. Wang, J. Fu, S. Wang, H. J. Zhang, and Y. C. Han. Fabrication, patterning, and optical properties of nanocrystalline $\text{YVO}_4:\text{A}$ ($\text{A} = \text{Eu}^{3+}, \text{Dy}^{3+}, \text{Sm}^{3+}, \text{Er}^{3+}$) phosphor films via sol-gel soft lithography. *Chem. Mater*, 14(5):2224–2231, 2002.
- [71] C. Powell Richard. *Physics of Solid State Laser Materials*. Springer Series in Materials Science, 1998.

- [72] E. De la Rosa-Cruz, L. A. Diaz-Torres, R. A. Rodriguez-Rojas, M. A. Meneses-Nava, and O. Barbosa-Garcia. Luminescence and visible upconversion in nanocrystalline $\text{ZrO}_2 : \text{Er}^{3+}$. *Appl. Phys. Lett*, 83:4903, 2003.
- [73] E. De la Rosa, L. A. Diaz-Torres, P. Salas, and R. A. Rodriguez. Visible light emission under uv and ir excitation of rare earth doped ZrO_2 nanophosphor. *Opt. Mat.*, 27:1320–1325, 2005.
- [74] P. Salas, C. Angeles-Chavez, J. A. Montoya, E. De la Rosa, L. A. Diaz-Torres, H. Desirena, A. Martinez, M. A. Romero-Romo, and J. Morales. Synthesis, characterization and luminescence properties of $\text{ZrO}_2 : \text{Yb}^{3+}\text{Er}^{3+}$ nanophosphor. *Opt. Mat.*, 27:1295–1300, 2005.